Colorado Plowable Hailstorms: Synoptic Weather, Radar, and Lightning Characteristics

EVAN A. KALINA,*,+ KATJA FRIEDRICH,# BRIAN C. MOTTA,@ WIEBKE DEIERLING,& GEOFFREY T. STANO,** AND NEZETTE N. RYDELL++

* *NOAA/Earth System Research Laboratory/Physical Sciences Division, Boulder, Colorado*
+ *NOAA/Atlantic Oceanographic and Meteorological Laboratory/Hurricane Research Division, Miami, Florida*
# *Department of Atmospheric and Oceanic Sciences, University of Colorado, Boulder, Colorado*
@ *NOAA/NWS/Office of the Chief Learning Officer, Boulder, Colorado*
& *National Center for Atmospheric Research, Boulder, Colorado*
** *NASA Short-term Prediction Research and Transition Center (SPoRT)/ENSCO, Inc., Huntsville, Alabama*
++ *NOAA/NWS, Boulder, Colorado*

(Manuscript received 19 March 2015, in final form 26 October 2015)

ABSTRACT

Synoptic weather, S-band dual-polarization radar, and total lightning observations are analyzed from four thunderstorms that produced "plowable" hail accumulations of 15–60 cm in localized areas of the Colorado Front Range. Results indicate that moist, relatively slow (5–15 m s^{-1}) southwesterly-to-westerly flow at 500 hPa and postfrontal low-level upslope flow, with 2-m dewpoint temperatures of 11°–19°C at 1200 LST, were present on each plowable hail day. This pattern resulted in column-integrated precipitable water values that were 132%–184% of the monthly means and freezing-level heights that were 100–700 m higher than average. Radar data indicate that between one and three maxima in reflectivity Z (68–75 dBZ) and 50-dBZ echo-top height (11–15 km MSL) occurred over the lifetime of each hailstorm. These maxima, which imply an enhancement in updraft strength, resulted in increased graupel and hail production and accumulating hail at the surface within 30 min of the highest echo tops. The hail core had $Z \sim 70$ dBZ, differential reflectivity Z_{DR} from 0 to −4 dB, and correlation coefficient ρ_{HV} of 0.80–0.95. Time–height plots reveal that these minima in Z_{DR} and ρ_{HV} gradually descended to the surface after originating at heights of 6–10 km MSL ~15–60 min prior to accumulating hailfall. Hail accumulations estimated from the radar data pinpoint the times and locations of plowable hail, with depths greater than 5 cm collocated with the plowable hail reports. Three of the four hail events were accompanied by lightning flash rates near the maximum observed thus far within the thunderstorm.

1. Introduction

Thunderstorms that result in deep hail accumulations pose a substantial risk to life and property. Numerous such hailstorms have resulted in motor vehicle accidents, road closures, airport delays, urban flooding, and water rescues (Chappell and Rodgers 1988; Grahame et al. 2009; Schlatter and Doesken 2010). Damage from one hailstorm, which produced 25 cm of hail accumulation in a small town in southwestern England on 30 October 2008, was estimated to cost 1 million British pounds [~1.8 million U.S. dollars in 2015; Grahame et al. (2009)]. A number of similar events have occurred in and near the Denver, Colorado, metropolitan area (Table 1; Knight et al. 2008; Schlatter et al. 2008; Schlatter and Doesken 2010), impacting thousands of people. Following the hailstorms, some roads, including major highways, remained impassable until snowplows and bulldozers were used to clear them (Fig. 1), leading these events to be called plowable hailstorms. Hail accumulations of 15–60 cm in 30 min occurred in these storms. However, the formation of hail drifts by strong winds and flowing water, especially at airports and on major roadways, could result in the need to plow smaller accumulations in other cases. Plowable hailstorms might also affect rural, agricultural areas where snowplows and

Corresponding author address: Evan A. Kalina, NOAA/Earth System Research Laboratory/Physical Sciences Division, 325 Broadway St., Boulder, CO 80305.
E-mail: evan.kalina@noaa.gov

DOI: 10.1175/WAF-D-15-0037.1

© 2016 American Meteorological Society

TABLE 1. Characteristics of CO plowable hailstorms during 2013–14 derived from the radar data, the CoCoRaHS network, and NOAA's Storm Events Database. Hail times and locations correspond to the plowable hail reports, and other severe weather (in addition to large hail) includes any tornadoes or wind gusts greater than 25 m s^{-1}. The storm speed was calculated from the change in position of the maximum reflectivity at $z = 5$ km MSL over the indicated analysis times.

Analysis time and date	Mean storm speed (m s^{-1})	Hail time and location	Max hail diameter (mm)	Other severe weather
1842–2356 UTC 3 Aug 2013	6.3	2216 UTC, Windsor	44.5	Three EF0 tornadoes; 25.7 m s^{-1} wind gust
2138–0021 UTC 22–23 Aug 2013	8.4	2339 UTC, Ken Caryl	44.5	None
1829–2258 UTC 9 Sep 2013	8.6	2100 UTC, Lakewood	12.7	None
1725–2247 UTC 21 May 2014	8.0	2030 UTC, Green Valley Ranch	25.4	Five EF0 tornadoes; 30.9 m s^{-1} wind gust

bulldozers are not in operation, causing such storms to remain undocumented.

Despite the extreme nature of these storms, some of the events, such as the 9 September 2013 hailstorm in Lakewood, Colorado (Table 1), did not merit a severe thunderstorm warning, since the maximum hailstone diameter ($d \sim 13$ mm) was much smaller than the warning criteria of 25.4 mm. Examples of similar events exist in the literature and were reported to consist of either small hail [$d < 10$ mm; Grahame et al. (2009)] or a mixture of low-density small and large hailstones (Knight et al. 2008; Schlatter et al. 2008). However, based on public reports from the Community Collaborative Rain, Hail, and Snow (CoCoRaHS) network[1] and the Storm Events Database[2], some of the plowable hailstorms were accompanied by large hail of up to 45 mm and did considerable damage to structures (e.g., Table 1: 3 August 2013 and 21 May 2014). Therefore, not all deep hail accumulations consist entirely of small- or low-density hailstones. In addition, severe wind gusts greater than 25 m s^{-1} and tornadoes can accompany plowable hailstorms (e.g., the 3 August and 21 May hailstorms in Table 1).

The considerable threats that accumulating hailstorms pose to people, transportation, and infrastructure require their accurate prediction. However, little is known about the synoptic weather conditions and operational radar features associated with thunderstorms that produce deep hail accumulations. The only case studies of such storms in the peer-reviewed literature consist of single-polarization radar data (Knight et al. 2008; Schlatter et al. 2008; Grahame et al. 2009). Therefore, dual-polarization radar characteristics of plowable hailstorms, available to forecasters since the 2012 upgrade to the Weather Surveillance Radar-1988 Doppler (WSR-88D) network, remain unexplored. This research examines the synoptic weather conditions and the radar and lightning characteristics of four plowable hailstorms that occurred along the Colorado Front Range between August 2013 and May 2014 (Fig. 2) to address several important questions: What are the typical synoptic weather conditions in which plowable hailstorms develop? How do storm propagation speed and hail duration affect hail accumulation? What are the typical radar features and derived products from the S-band operational radar network that characterize plowable hailstorms? Are there other state-of-the-art instruments, such as three-dimensional total lightning detection networks, that can provide additional insight into the microphysical processes that contribute to plowable hail? Are the radar and lightning signatures sufficient to nowcast accumulating hailstorms? To our knowledge, this is the first study to present such a comprehensive analysis on plowable hailstorms.

2. Background

The S-band dual-polarization radar characteristics of severe thunderstorms with large hail are well documented. Radar reflectivity Z is often used to identify hailstorms because it is proportional to the sixth power of the particle diameter. Typically, Z exceeds 60 dBZ in hailstorms (Kumjian and Ryzhkov 2008; Snyder et al. 2010). Storms containing giant hail ($d > 50.8$ mm) have $Z > 65$–70 dBZ (Ryzhkov et al. 2010). For a given hailstone size, Z is larger for hailstones with greater fractional water content, since the liquid water coating that develops on hailstones undergoing wet growth is highly reflective (Snyder et al. 2010). Therefore, wet hail and giant hail may be associated with similar Z values, requiring the use of differential reflectivity Z_{DR} to distinguish between the two, where Z_{DR} is the logarithmic ratio of the reflectivities in the horizontally and vertically polarized channels. Giant hail ($d > 50.8$ mm) is typically characterized by $Z_{DR} < -0.5$ dB (Ryzhkov et al. 2010). The Z_{DR} measurements of large hail

[1] http://www.cocorahs.org/.
[2] Information online at http://www.ncdc.noaa.gov/stormevents/.

FIG. 1. Hail being plowed in Lakewood after the 9 Sep 2013 hailstorm. (Reprinted with permission. Photo credit: 7NEWS Denver reporter M. Zelinger.)

($25.4 \leq d \leq 50.8$ mm) are near 0 dB (Balakrishnan and Zrnić 1990b; Kumjian and Ryzhkov 2008; Snyder et al. 2010; Kennedy et al. 2014), as a result of the tumbling nature of hailstones (Lesins and List 1986; Herzegh and Jameson 1992). Finally, small ($d < 25.4$ mm), wet hail has $Z_{DR} > 0$ dB, sometimes exceeding 4 dB (Ryzhkov et al. 2013a), because of the coating of liquid water that envelopes the melting hailstones (Rasmussen and Heymsfield 1987). A third radar variable, the copolar cross-correlation coefficient ρ_{HV}, can also be used to identify hail. Values of ρ_{HV} range from zero to one and quantify the degree of similarity in the shape and orientation of particles within the radar volume. In rain, ρ_{HV} normally exceeds 0.97, but in hail, ρ_{HV} can range from 0.8 to 0.95 because of the diversity of shapes and orientations typical of hailstones (Ryzhkov et al. 2013b). The largest reductions in ρ_{HV} occur when large hail is mixed with rain in the radar volume (Balakrishnan and Zrnić 1990b). Finally, the specific differential phase K_{DP}, the rate of change in the phase difference between horizontally and vertically polarized waves, is $0° \text{ km}^{-1}$ for a radar volume that contains dry, spherical hailstones, but can exceed $5° \text{ km}^{-1}$ for a mixture of oblate raindrops and water-coated, melting hail (Balakrishnan and Zrnić 1990a).

There are also classic radar signatures in the three-dimensional Z and Doppler velocity fields that can be used to identify severe hailstorms. Thunderstorms that produce large hail often contain a weak-echo region (WER) that coincides with the main updraft (e.g., Browning and Ludlam 1962; Browning 1965; Marwitz and Berry 1971; Marwitz et al. 1972). Here, strong vertical velocities within the updraft evacuate rain and graupel particles before they can grow sufficiently to create a substantial radar echo. The WER extends vertically from the near surface into the midlevels of the storm and is usually capped by an overhang of rain and hail. If this overhang is so extensive that it bounds the WER on all sides (except below it), the WER is termed a bounded weak-echo region (BWER). Although BWERs are sometimes observed in multicell storms when individual updrafts in the cluster reach their maturity, the most persistent and steady BWERs typically occur in supercell thunderstorms (Knight and Knight 2001). The airflow in these rotating storms favors hailstone embryo recycling (Browning 1963; Browning and Foote 1976; Nelson 1983; Knight and Knight 2001; Tessendorf et al. 2005). Briefly, embryos (i.e., rain and graupel particles) enter the updraft within the low-level inflow and are carried aloft to a position above the BWER. Lighter particles are then carried downwind when they encounter the midlevel airflow, while heavier particles descend, circulating around the BWER and potentially recycling into the inflow to undergo additional growth. The latter trajectory results in large hail formation.

In addition to radar signatures that imply the presence of hail, a number of studies have shown that in some thunderstorms increases in lightning flash rate precede severe weather events, including hailfall, by 5–20 min

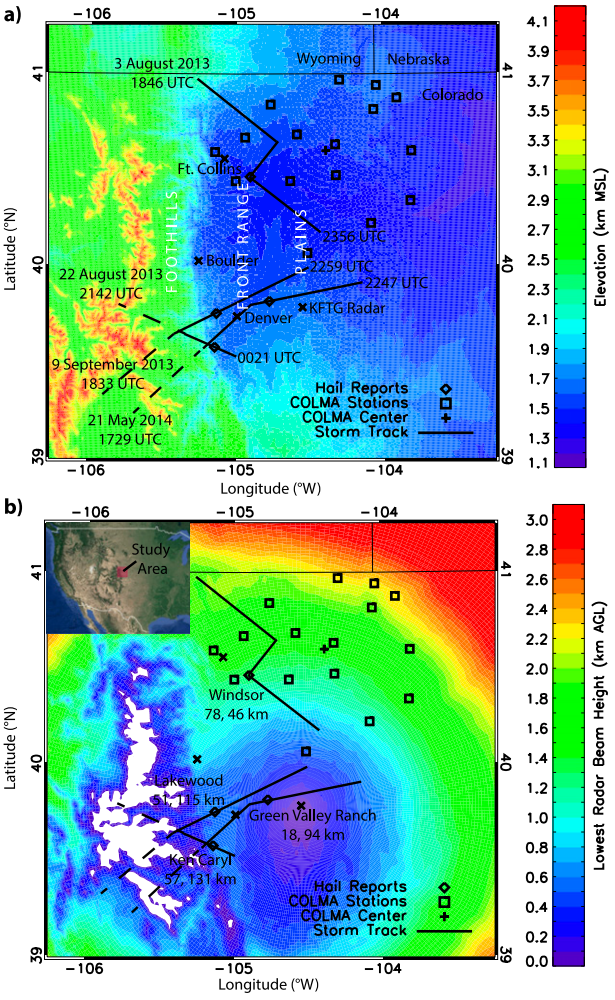

FIG. 2. Maps showing the locations of hail reports (diamonds), cities and the KFTG radar (crosses), COLMA stations (squares), the center of COLMA (plus sign), and the approximate storm tracks (lines) relative to (a) the elevation of the topography (km MSL) and (b) the height of the center of the lowest radar beam (km AGL). Dashed lines indicate areas of beam blockage along the storm tracks. The numbers in (a) indicate the start and end times (UTC) of the analysis periods for each case and in (b) the distances (km) from the plowable hail reports to the KFTG radar (cross) and to the COLMA center (plus sign), respectively. The names of the plowable hail report locations are given in (b).

(e.g., Williams et al. 1999; Goodman et al. 2005; Wiens et al. 2005; Schultz et al. 2009; Darden et al. 2010; Rudlosky and Fuelberg 2013). This is despite the fact that thunderstorm charging can be locally reduced in regions of wet hail growth (Saunders and Brooks 1992; Pereyra et al. 2000; Emersic et al. 2011), likely because of the reduced number of rebounding collisions between water-coated graupel and ice crystals. Lightning flash rate also has been found to be correlated with updraft strength, updraft volume, and graupel mass (e.g., Carey and Rutledge 1996; Wiens 2005; Wiens et al. 2005; Tessendorf et al. 2007; Deierling and Petersen 2008; Deierling et al. 2008). Thus, lightning data can help forecasters assess thunderstorm intensity and determine whether a storm is in the developing, mature, or weakening phases of its life cycle (Darden et al. 2010; Rudlosky and Fuelberg 2013). The lightning characteristics of plowable hailstorms, however, have yet to be investigated, raising the following question: Do increases in lightning flash rate precede the occurrence of accumulating hail, even in cases when the hailstones are too small to be classified as severe? This study examines three-dimensional total lightning data from four plowable hailstorms to determine if this information can aid forecasters in predicting similar future events.

3. Data and methods

a. Overview of cases

The hailstorms analyzed in this research occurred in August–September 2013 and May 2014 along the Colorado Front Range and produced hail accumulations of at least 15 cm within 30 min. Figure 2 depicts the approximate storm tracks[3] in relation to the local topography, while Table 1 provides the locations and times of the plowable hail reports. With the exception of the 9 September case, these hailstorms were considered severe thunderstorms, as two of the storms produced severe wind gusts and multiple tornadoes rated on the Enhanced Fujita (EF) scale as EF0 events (3 August and 21 May) and all but the 9 September case produced large hail (Table 1). The maximum diameter of the hailstones ranged from 12.7 to 44.5 mm during hail accumulation. The location, time, and maximum diameter of the hailstones are based on data from the CoCoRaHS network and the Storm Events Database. The latter contains the data used to create NOAA's monthly *Storm Data* publication, which documents the time, location, number of casualties, and amount of property damage associated with severe and unusual weather events in the United States. Based on these data and reports from multiple media outlets, maximum hail depths were estimated to range from 15 to 60 cm in the four storms. However, there is considerable uncertainty in the maximum depth produced by any one particular storm as a result of limited observations and the lack of standards for measuring hail depth. This study focuses on four examples of plowable hailstorms that occurred in 2013 and

[3] A cell merger produced the unusual track of the 3 August storm, causing it to temporarily deviate toward the southwest.

2014. We are aware of nine plowable hailstorms along the Colorado Front Range from June 2012 to September 2014 and at least six additional cases from April to May 2015 that occurred after this analysis was completed.

b. Radar data and operational soundings

Dual-polarization radar data were obtained from the WSR-88D located at Front Range Airport (KFTG; Fig. 2; 1.68 km MSL) for each of the thunderstorms in Table 1. The radar was operated in velocity coverage pattern 212, and scanned 14 elevation angles from 0.5° to 19.5° (OFCM 2013). In all cases, $Z > 0$ dBZ was first observed to the west of KFTG at a distance of 111–152 km from the radar site, and Z then gradually increased as the storms approached the radar. The minimum distance between the center of the storms and the radar ranged from 9 to 44 km during the analysis periods. At the time of the plowable hail reports, the distances from the radar ranged from 18 km (21 May) to 78 km (3 August), which caused the height of the lowest radar beam (0.5° elevation angle) to range from 0.2 to 1.3 km AGL (Fig. 2b). The data analysis period for each storm began when $Z > 0$ dBZ in the eventual hailstorm first appeared in the radar volume. Analysis continued until the convective core of the hailstorm (defined herein as $Z > 30$ dBZ) merged with other convective cores and became indistinguishable in the radar data. This occurred as little (long) as 39 (138) min after the plowable hail report time.

All radar volumes during the periods of analysis were manually edited with the Solo II radar software[4] from the National Center for Atmospheric Research (NCAR) to remove echoes unrelated to the plowable hailstorms, including echoes from nonmeteorological targets such as ground clutter and precipitation in the vicinity of the hailstorms but unrelated to them. Following the results of Giuli et al. (1991) and Park et al. (2009), several radar variables (i.e., Z, Doppler velocity V_r, spectrum width W, and Z_{DR}) were used to identify nonmeteorological targets. Each elevation angle in the radar volume was examined individually, because thunderstorm echoes were often tilted with height. Ground clutter that was not removed by the radar signal processor was visually identified by radar gates that contained nearly constant Z over time, V_r near 0 m s^{-1}, and $W > 8$ m s^{-1}. The latter criterion was used to identify the boundary between radar gates that contained pure clutter and those that contained a mixture of weather echoes and clutter. Other nonmeteorological echoes, which consisted mainly of biological scatterers, were visually identified by radar gates that had $Z < 25$ dBZ and spatially inhomogeneous $Z_{DR} > 4$ dB (Park et al. 2009). When showers and thunderstorms other than the hailstorm occurred in the radar volume, these echoes were removed unless the convective core ($Z > 30$ dBZ) of the shower or thunderstorm merged with the convective core of the hailstorm at the lowest elevation angle (0.5°). Areas of precipitation consisting entirely of $Z < 30$ dBZ that were not contiguous with the hailstorm at 0.5° elevation angle were removed.

After editing the radar data, NCAR's Radx C++ software package[5] was used to calculate K_{DP} from the total differential phase Φ_{DP} measured by the radar. To calculate K_{DP}, a finite impulse response filter with a length of 10 range gates was iteratively applied to Φ_{DP} four times to smooth it. Then, K_{DP} was calculated from the smoothed Φ_{DP} over nine range gates, centered on the gate of interest. Next, the NCAR particle identification scheme (PID; Vivekanandan et al. 1999) was applied to the data. The PID is a fuzzy logic algorithm that uses trapezoidal membership functions for seven input variables and 14 particle classes to estimate the most dominant contributor to the radar signal in each range gate. The PID input variables are Z, Z_{DR}, K_{DP}, ρ_{HV}, standard deviation of Z_{DR} and Φ_{DP} (calculated over nine range gates), and air temperature. Air temperature profiles were obtained from the 0000 UTC atmospheric soundings at Denver during the evenings of the plowable hail cases, except for the 21 May case, when an 1800 UTC sounding was available (Table 2). For each of the aforementioned input variables, the PID assigns a value between zero and one to each range gate for each of the following particle classes: cloud droplets, drizzle, light rain, moderate rain, heavy rain, rain–hail mix, hail, graupel–small hail mix, graupel–rain mix, dry snow, wet snow, ice crystals, irregular ice crystals, and supercooled liquid droplets. The seven values belonging to a given particle class are then summed, and the class with the largest sum is assigned to the radar gate.

The Radx software package was then used to regrid the polar coordinate radar data to a Cartesian coordinate system using an eight-point linear interpolation scheme. The azimuthal equidistant map projection was selected for the Cartesian grid, which spanned 400 × 400 km^2 in the horizontal and 15 km MSL in the vertical, with the KFTG radar located at the grid center. Each grid cell had horizontal and vertical dimensions of 0.5 km. To interpolate the radar variables onto a given

[4] Information online at https://www.eol.ucar.edu/software/solo-ii.

[5] Information online at http://www.ral.ucar.edu/projects/titan/docs/radial_formats/radx.html.

TABLE 2. Surface-based CAPE (SBCAPE), 0–6 km AGL bulk shear, BRN, PWAT, and 0–6 km AGL mean wind derived from Denver rawinsonde soundings (Fig. 6) for the cases listed in Table 1.

Time (environment)	SBCAPE ($J\,kg^{-1}$)	Bulk shear ($m\,s^{-1}$)	BRN	PWAT (mm)	Mean wind vector (°/$m\,s^{-1}$)
0000 UTC 4 Aug 2013 (storm outflow)	1022	18.4	8.1	28.5	228/5.3
0000 UTC 23 Aug 2013 (prestorm)	2568	17.6	296	32.6	249/1.8
0000 UTC 10 Sep 2013 (storm outflow)	1342	18.6	11.2	30.8	211/4.4
1800 UTC 21 May 2014 (prestorm)	1740	18.7	28.1	15.8	212/11.9

grid cell, a minimum of five valid data points (out of a possible eight) needed to be present. Since the PID is a discrete field, it was not interpolated and was instead assigned to each grid cell using the nearest neighbor approximation.

Graupel M_g and hail M_h mass concentrations ($g\,m^{-3}$) were then estimated from the radar reflectivity Z ($mm^6\,m^{-3}$) using the relations from Heymsfield and Miller (1988):

$$M_g = 0.0052Z^{0.5} \quad \text{and} \tag{1}$$

$$M_h = 0.000\,044Z^{0.71}. \tag{2}$$

The graupel relation was applied to all of the radar cells that were classified by the PID as graupel/small hail or graupel/small hail/rain mix, while the hail relation was applied to all of the grid cells classified as hail or hail/rain mix, as in Deierling et al. (2008). Equations (1) and (2) were derived from in situ aircraft measurements of ice particle size spectra ($0.0125 < d < 40$ mm) in the updrafts of a single-cell thunderstorm [Eq. (1)] and a supercell thunderstorm [Eq. (2)]. These storms occurred in eastern Montana, an environment that is geographically and climatologically similar to eastern Colorado. These Z–M relationships have been applied to a variety of single-cell, multicell, and supercell thunderstorms across the United States (Deierling et al. 2008). While it is acknowledged that large absolute errors in ice mass estimates from these relations likely exist, the focus of our study is not on the absolute values of the ice masses but on the relative changes in these masses over the hailstorm lifetimes.

c. Lightning data

The Colorado Lightning Mapping Array (COLMA; Rison et al. 2012) was installed in spring 2012 and provided three-dimensional lightning data. The array consists of 16 stations in northern Colorado (Fig. 2). Each station is equipped with a receiving antenna that is sensitive to very high frequency (VHF) radiation of ~60 MHz, a frequency at which portions of lightning discharges emit strongly. The location (x, y, z) and time t of a VHF source is determined from time-of-arrival t_i information recorded by global positioning system receivers at multiple COLMA stations:

$$t_i = t + \sqrt{\frac{(x - x_i)^2 + (y - y_i)^2 + (z - z_i)^2}{c}}. \tag{3}$$

Above, the location of the receiving station is (x_i, y_i, z_i) and c is the propagation speed of the VHF radiation. If t_i is measured by at least four stations, the four unknowns x, y, z, and t can be determined from Eq. (3). The errors in the radial and vertical positions of VHF sources are proportional to $(r/D)^2$ and $(z/D)^2$, respectively, where r is the radial distance from the array center to the lightning source, z is the altitude of the source, and D is the diameter of COLMA (~100 km). COLMA is capable of detecting lightning sources up to 350 km away from the array center (Rison et al. 2012), which includes the entire domain shown in Fig. 2. At the time of the plowable hail reports, the distance of the storms from the array center ranged from 46 to 131 km (Fig. 2b).

The individual VHF sources were processed with the McCaul et al. (2005, 2009) flash creation algorithm to filter out noise sources and to combine the remaining sources into lightning flashes. Sources were assumed to be part of the same lightning flash if they satisfied certain temporal and spatial criteria. First, the sources must have occurred within 0.3 s of each other to be grouped into the same flash. Next, the radial distance between successive sources must not have exceeded $r^2/1000$. For example, the maximum allowable radial distance between sources at 200-km range was 40 km (McCaul et al. 2009). This criterion reflects the dependence of the error in the radial position of a source on its radial distance from the array center. Additionally, sources were not allowed to be more than 0.05 rad (~2.9°) apart in azimuth (the maximum expected azimuth error) to be grouped into the same flash. To prevent noise sources from bridging the time and/or distance between two separate flashes, sources with arrival times that had reduced chi-square goodness-of-fit values [described in Thomas et al. (2004); their Eq. (A2)] of more than 2.0 were not grouped into flashes. In addition, flashes with fewer than 10 sources were

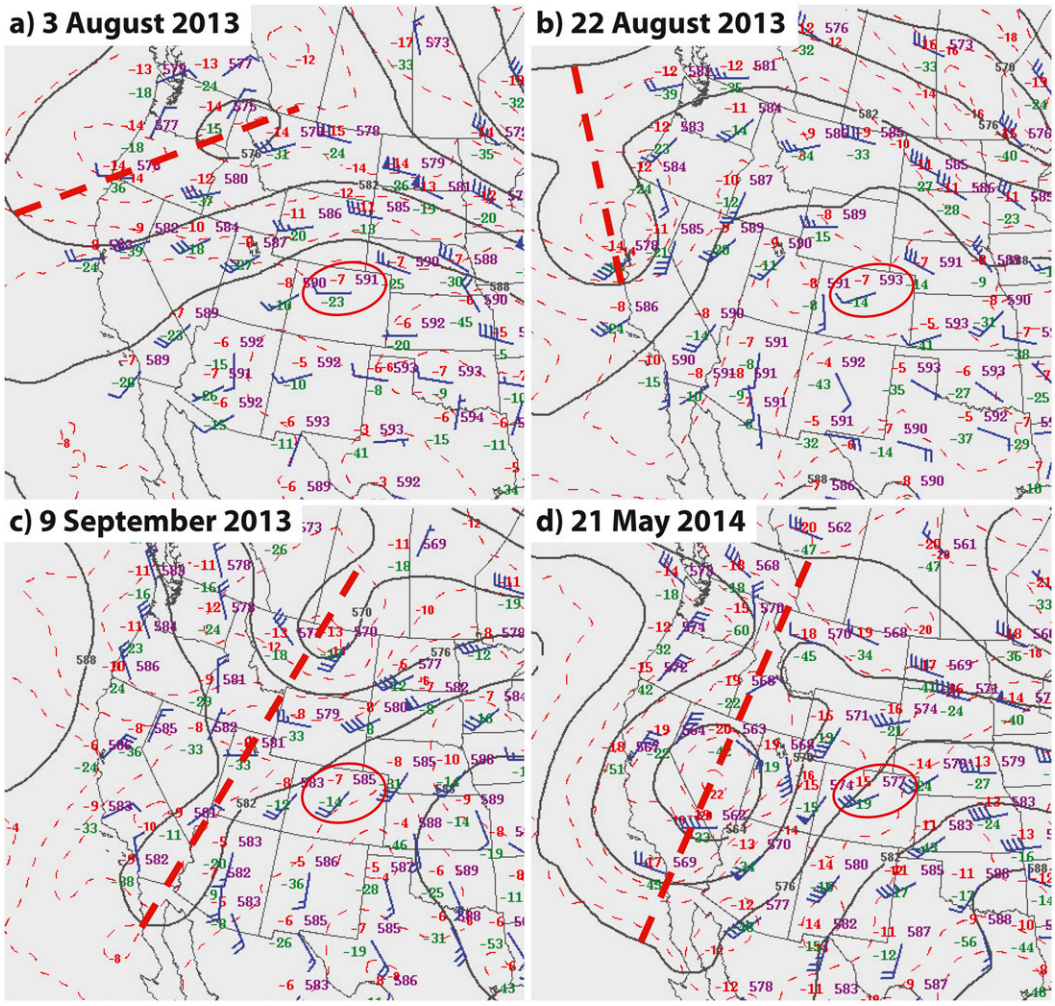

FIG. 3. Observations at the 500-hPa pressure level at 1200 UTC: air temperature (°C, red numbers), dewpoint temperature (°C, green numbers), geopotential height (dm, purple numbers), and wind barbs [knots (kt), where 1 kt = 0.51 m s^{-1}; blue] on (a) 3 Aug 2013, (b) 22 Aug 2013, (c) 9 Sep 2013, and (d) 21 May 2014. Temperature (dashed thin red lines) and height (black lines) are contoured at intervals of 2°C and 6 dm, respectively. Dashed thick red lines denote the positions of trough axes. The Denver observation is circled in red.

eliminated from the data, as in Wiens et al. (2005) and Tessendorf et al. (2007).

Following lightning flash creation, the sources from each flash were gridded into a Cartesian volume identical to that used for the radar data (section 3b). To exclude lightning flashes from all thunderstorms other than the plowable hailstorm, the initial source of each flash was checked to determine if it was located within a vertical column of the Cartesian radar data that had $Z \geq 0$ dBZ somewhere within that column (after other precipitation and nonmeteorological echoes were removed). Flashes with initial sources in regions of $Z < 0$ dBZ were excluded. One-minute flash rates and individual flash areas were then calculated from the remaining flashes. Flash area was estimated by counting the number of grid cells that contained at least one lightning source from the flash under consideration and then multiplying the total count by the area of one grid cell (0.25 km^2).

4. Results

a. *Meteorological conditions*

This section examines the synoptic and mesoscale weather conditions that favored hail accumulations in the four thunderstorms in Table 1. Figure 3 shows the 500-hPa height, air temperature, dewpoint temperature, and wind vectors measured by rawinsondes at 1200 UTC on the morning of each hailstorm. Anticyclonic curvature in the wind field over Colorado is evident on all four days as a result of a ridge of high pressure. However, the position of the ridge axis

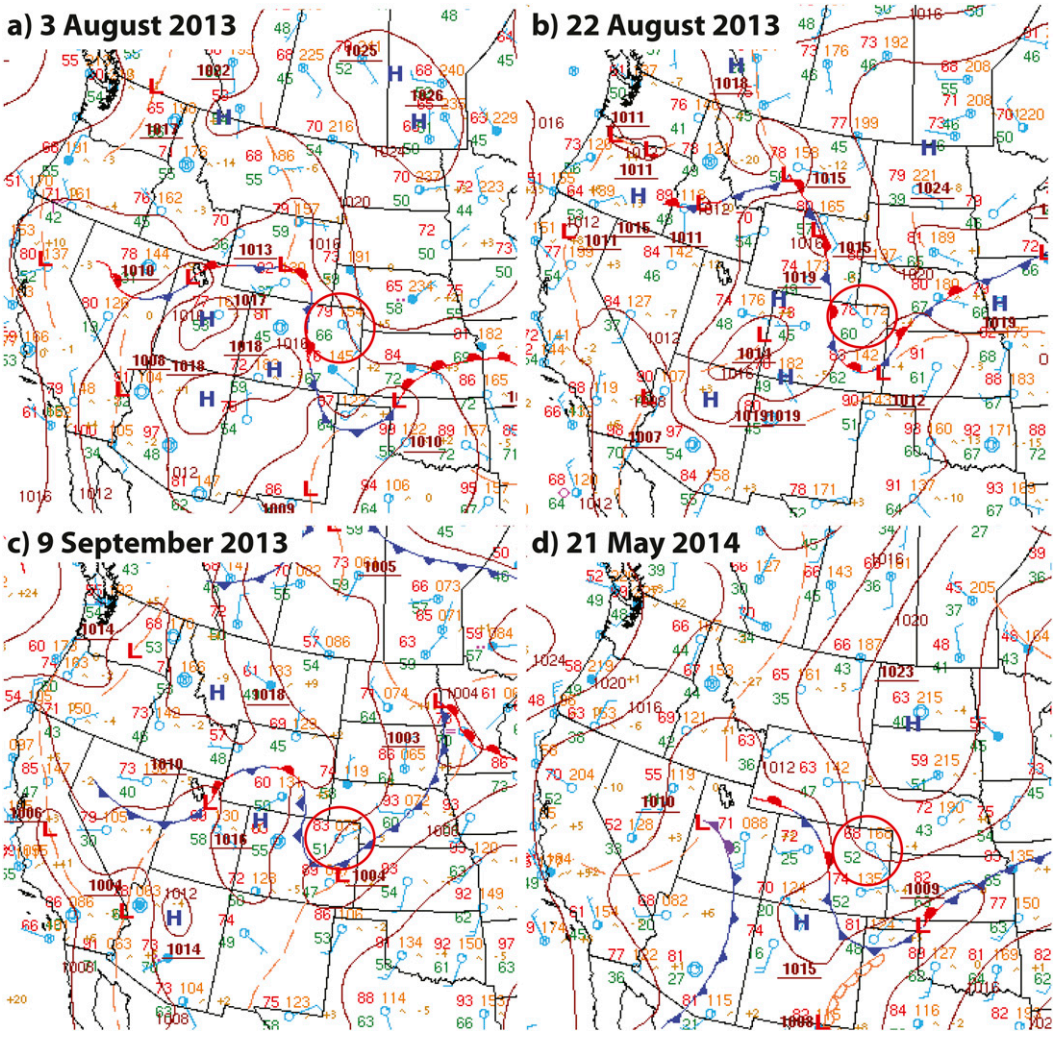

FIG. 4. Surface observations at 1800 UTC: air temperature (°F, red numbers), dewpoint temperature (°F, green numbers), mean sea level pressure (hPa, large tan numbers), mean sea level pressure change relative to 3 h earlier (10 × hPa, small tan numbers), and wind barbs (kt, blue) on (a) 3 Aug 2013, (b) 22 Aug 2013, (c) 9 Sep 2013, and (d) 21 May 2014. Mean sea level pressure (brown lines) is contoured at intervals of 4 hPa. Frontal boundaries, trough axes, drylines, and high and low pressure systems are denoted by their standard symbols at the surface. The Akron–Washington County Airport, CO (~130 km east of Denver), observation is circled in red.

differed on the first two days (3 August and 22 August; Figs. 3a,b) compared with the latter two days (9 September and 21 May; Figs. 3c,d). On 3 and 22 August, a ridge axis was aligned north–south across central Colorado with lower heights to the west across Utah and Nevada. In contrast, an upper-level trough and closed upper-level low were approaching Colorado on 9 September (Fig. 3c) and 21 May (Fig. 3d), respectively. These weather features resulted in 500-hPa winds from the southwest or west at 5–15 m s^{-1} at Denver (KDEN) on each of the four days. The light-to-moderate southwesterly flow transported a plume of midlevel subtropical moisture northward from the eastern Pacific, as evidenced by 500-hPa dewpoint depressions of ≤7°C (except on 3 August; Fig. 3a).

In addition to similarities in the mid- and upper-level patterns, the near-surface synoptic weather features were also similar for the hailstorms. Figure 4 demonstrates that all four cases occurred in low-level easterly upslope flow behind a cold front that moved through eastern Colorado earlier in the day. The upslope flow moistened the low-level air mass, resulting in 2-m dewpoint temperatures that ranged from 11°C (51°F) on 9 September (Fig. 4c) to 19°C (66°F) on 3 August (Fig. 4a) at 1800 UTC (1200 LST) over eastern Colorado. Warm near-surface air temperatures of 20°–28°C

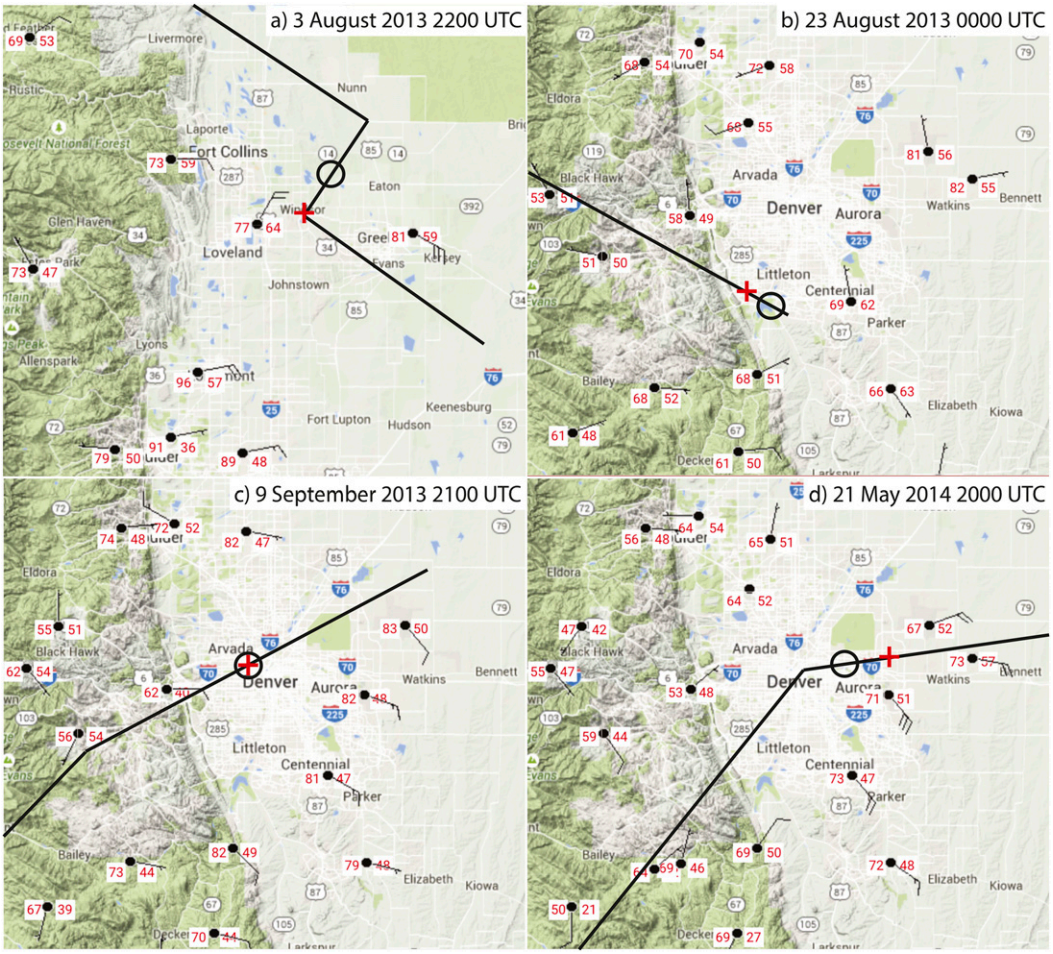

FIG. 5. Surface observations near the time that plowable hail occurred: air temperature (°F, left of wind barb), dewpoint temperature (°F, right of wind barb), and wind barbs (kt) at (a) 2200 UTC 3 Aug 2013, (b) 0000 UTC 23 Aug 2013, (c) 2100 UTC 9 Sep 2013, and (d) 2000 UTC 21 May 2014. The black lines show the approximate tracks of the hailstorms. Open circles and red plus signs indicate the storm locations at the analysis times and the plowable hail report locations, respectively.

accompanied the low-level moisture (Fig. 4). Figure 5 shows surface observations near the plowable hail times and demonstrates that the warm, moist low-level environment across northeast Colorado persisted throughout the day. Temperatures downwind of the storms ranged from 21°C (69°F) to 28°C (83°F), with dewpoint temperatures from 10°C (50°F) to 18°C (64°F). Except in the 22 August case, easterly-to-southeasterly inflow winds of 10–20 m s^{-1} were present in the near-storm environment over the eastern plains (Fig. 5), suggestive of enhanced low-level convergence closer to the foothills (where light and variable winds were present). The low-level easterly flow and the weak-to-moderate midlevel westerly winds produced mean 0–6 km AGL [i.e., steering layer; Weisman and Klemp (1984)] winds of 1.8–11.9 m s^{-1}, as calculated from KDEN atmospheric soundings (Table 2 and Figs. 6 and 7). These light steering winds resulted in slow mean storm motions of 6–9 m s^{-1} (calculated from radar imagery; Table 1), which favored hail accumulations. The role of storm propagation speed in plowable hail events is discussed more fully in section 5.

The warm, moist low-level air also resulted in surface-based convective available potential energy (CAPE) values from 1022 to 2568 J kg^{-1} at KDEN during the afternoons of the hailstorms (Table 2). The two soundings (3 August and 9 September) with the smallest CAPE values (1022 and 1342 J kg^{-1}) occurred in storm outflow, which suggests that the CAPE may have been even larger on these days. In regard to the vertical wind shear, the low-level easterly upslope flow that gradually veered and strengthened to midlevel westerly flow of 10–25 m s^{-1} (Fig. 6) contributed to 0–6 km AGL bulk wind shear of ~18 m s^{-1} during each

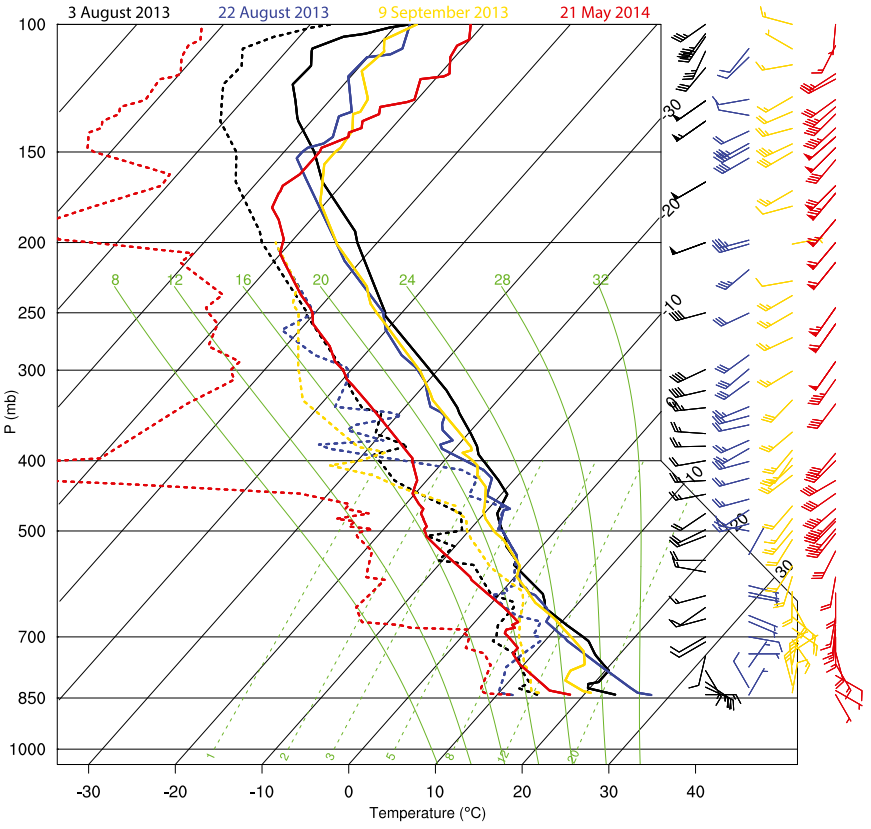

FIG. 6. Skew T–log$p$ diagram with air temperature (solid lines), dewpoint temperature (dotted lines), and wind velocity (barbs) at KDEN on (a) 0000 UTC 4 Aug 2013 (black), (b) 0000 UTC 23 Aug 2013 (blue), (c) 0000 UTC 10 Sep 2013 (gold), and (d) 1800 UTC 21 May 2014 (red).

event (Table 2). Hodographs illustrate the cyclonically curved flow with height that was evident within the lowest 3 km during each of the cases, as well as the tendency for slow storm motions (Fig. 7). This combination of vertical wind shear and instability prompted tornado watches to be issued for northeast Colorado on 3 August and 21 May, with the watches mentioning the favorable environment for supercell thunderstorms. The bulk Richardson number (BRN; Table 2) calculated from the afternoon soundings (Fig. 6) supports this assessment, with values of 8.1 (3 August) and 28.1 (21 May) indicative of supercellular convection [BRN < 45; Weisman and Klemp (1984)]. On the other two days (22 August and 9 September), mesoscale discussions issued by the Storm Prediction Center mentioned the possibility of organized multicell storm clusters capable of severe wind and hail. While the BRN from the sounding on 22 August (296) supports the expectation of multicells, the BRN of 11.2 on 9 September is suggestive of supercell thunderstorms.

In agreement with the convective modes predicted by the BRN, only the hailstorm on 22 August lacked supercell thunderstorm characteristics. The other storms all turned to the right of the mean 0–6-km wind vector as they intensified (Fig. 2), and radar data (discussed in the next section) displayed evidence of inflow notches, hook echoes, and BWERs. The 3 August and 21 May storms also produced a combined total of eight EF0 tornadoes (Table 1). Thus, the supercell thunderstorm mode of hail production (Browning 1963; Browning and Foote 1976; Nelson 1983; Knight and Knight 2001; Tessendorf et al. 2005), in which graupel and frozen raindrops circulate repeatedly through the updraft and inflow regions of the thunderstorm (termed embryo recycling), may have supported the development of large quantities of hail in three of the four cases considered herein. Strongly sheared environments also have been shown to prolong the residence time of hailstones within the thunderstorm updraft (Dessens 1960; Das 1962; Longley and Thompson 1965; Berthet et al. 2013), further contributing to hail mass.

Each of the hailstorms occurred on days with large amounts of atmospheric moisture, with column-integrated precipitable water vapor (PWAT) values

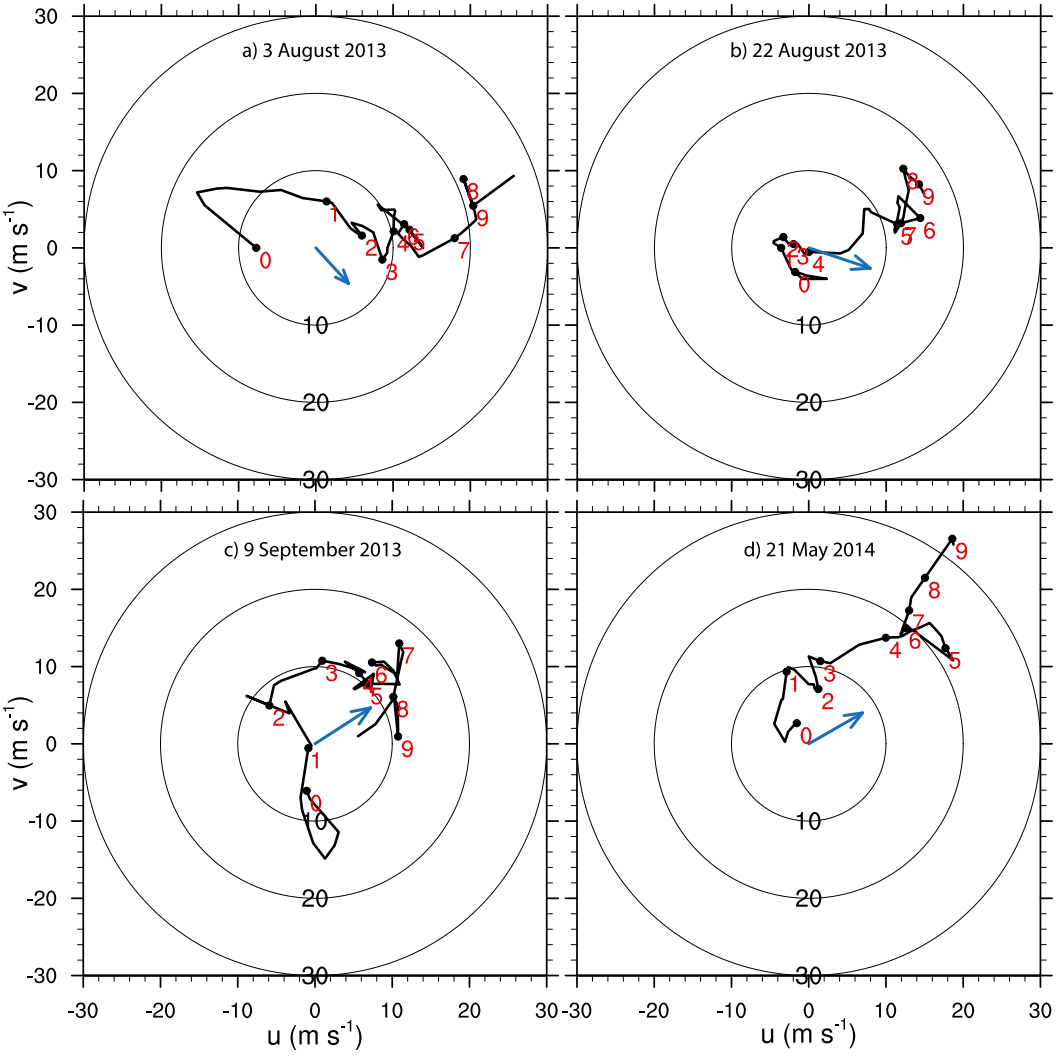

FIG. 7. Hodographs of the wind profiles observed by radiosonde launches at KDEN (Fig. 6) at (a) 0000 UTC 4 Aug 2013, (b) 0000 UTC 23 Aug 2013, (c) 0000 UTC 10 Sep 2013, and (d) 1800 UTC 21 May 2014. The red numbers indicate the height above the surface (in km), and the black numbers along the concentric circles indicate the wind speed (in m s^{-1}). The blue arrows represent the observed storm motion vectors of the plowable hailstorms.

that ranged from 19 to 33 mm (Fig. 8a). PWAT values were calculated from the rawinsonde soundings at KDEN during the mornings (1200 UTC) and evenings (0000 UTC) of the hailstorms. To put into perspective how anomalous these PWAT values were, Fig. 8a compares the measured PWAT to monthly mean values from 1957 to 2014. These means were calculated from 0000 and 1200 UTC KDEN rawinsonde profiles that had nonzero mixed-layer CAPE (to exclude soundings unlikely to be supportive of deep convection), which resulted in 1400–2100 profiles in each monthly sample. Maximum PWAT on the plowable hail days ranged from 132% to 184% of the monthly means (Fig. 8a). In fact, the morning sounding on 21 May and the evening soundings on 22 August and 9 September had PWAT values that were near or greater than two standard deviations above average. The anomalously large atmospheric moisture is further highlighted by the 9 September event, which marked the beginning of the Great Colorado Flood (9–16 September 2013) that resulted from over 400 mm of rainfall in localized areas of the Colorado Front Range (Friedrich et al. 2016a,b; Gochis et al. 2015). These events suggest that, at least in eastern Colorado, large PWAT may be a necessary (but not sufficient) condition for plowable hailstorms to occur. Such storms may be more likely on days in which forecasters also expect a flash flood risk from slow-moving thunderstorms, if sufficient instability and wind shear are present for sustained, intense updrafts.

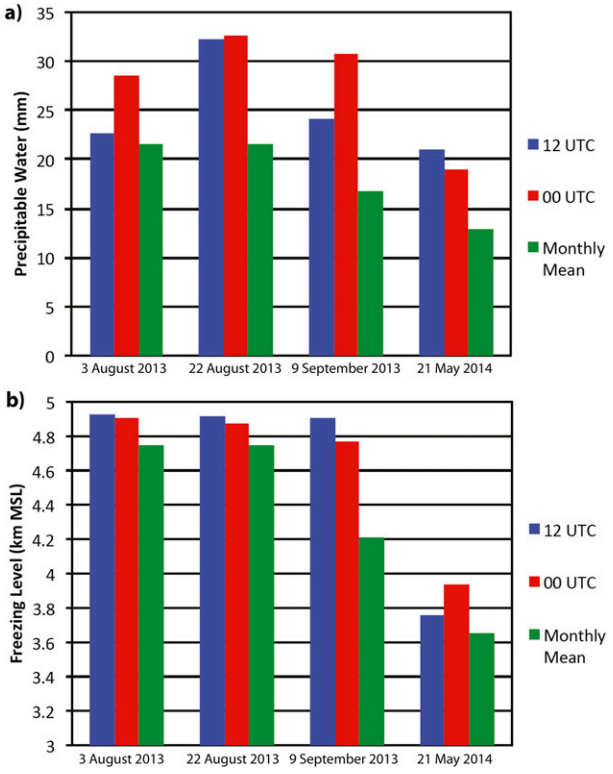

FIG. 8. Bar plots of (a) column-integrated precipitable water vapor and (b) freezing-level height from KDEN rawinsondes at 1200 UTC on the morning of the plowable hailstorm (blue) and at 0000 UTC on the evening of the plowable hailstorm (red). The green bars indicate monthly mean values of precipitable water and freezing-level height calculated from all 1200 and 0000 UTC KDEN rawinsondes from 1957 to 2014 that had mixed-layer CAPE greater than 0 J kg^{-1}.

Because low freezing-level heights are frequently associated with hailstorms (e.g., Pappas 1962; Xie et al. 2010), we also investigated whether the freezing-level heights were anomalously low on the plowable hail days. The freezing-level height was calculated from KDEN soundings during the mornings and evenings of the hailstorms and compared to the 1957–2014 monthly mean freezing-level heights, as calculated from the 0000 and 1200 UTC KDEN rawinsonde profiles that had nonzero mixed-layer CAPE in those years. This comparison reveals that the freezing-level height was 100–700 m higher than average on the plowable hail days (Fig. 8b). While low freezing-level heights are often associated with large hail events, the Clausius–Clapeyron relation suggests that the freezing level is likely to be higher than average when anomalously large atmospheric moisture is present, as in these cases. Therefore, low freezing-level heights may not be associated with plowable hail days in eastern Colorado.

b. Radar analysis

1) Description of radar features in each hailstorm

(i) 3 August 2013 supercell thunderstorm

We first examine radar data from the long-lived tornadic supercell that produced accumulating hail in Windsor, Colorado (Table 1; Fig. 2b). At the plowable hail report time (2216 UTC), the 3 August storm had near-surface $Z > 70$ dBZ (Fig. 9a), an unusually large value in the absence of giant hail ($d > 50.8$ mm) and likely indicative of the extreme hail mass concentration. A low-level inflow notch is also evident in Z, indicative of the supercell structure. The Z_{DR} and ρ_{HV} constant-altitude plan position indicators (CAPPIs) at the lowest available radar height ($z = 3.5$ km) depict minimum values from 0 to −1 dB (Fig. 10a) and 0.80 to 0.95 (Fig. 11a) within the maximum reflectivity region (black contours in Figs. 9–12), respectively. The K_{DP} values ranged from 0° to 2° km^{-1} (Fig. 12a), suggestive of large numbers of spherical hailstones.

Vertical cross sections of Z (Fig. 13) provide insight into the hailstorm life cycle and the period of intensification that resulted in accumulating hail. From 2157 to 2211 UTC, the storm intensified rapidly as 50-dBZ echo-top heights increased from $z = 8$ to 13 km and a BWER began to form (Figs. 13a–c). The plowable hail report at 2216 UTC occurred 5 min after the BWER became evident (Fig. 13c) and coincided with a peak in 50-dBZ echo-top height of ~13.5 km (Figs. 13c and 14a), increased hail production ($>6 \times 10^7$ kg; Fig. 14a), and maximum column $Z > 71$ dBZ (Fig. 14a). These metrics then became less impressive within 30 min of the hail report, and the BWER weakened and was no longer present by 2225 UTC (Fig. 13d). Taking a broader view of the hailstorm life cycle, two other maxima in intensity (labeled 1 and 2 in Fig. 14a) similar to the one described above are evident in the time–height cross section of Z, but it is not possible to know whether these events produced accumulating hail as a result of the lack of hail depth observations.

Time–height plots of the dual-polarization radar variables (Figs. 15–17) reveal a number of times when minimum $Z_{DR} < -2.5$ dB (Fig. 15a) and $\rho_{HV} < 0.75$ (Fig. 16a) overlapped with each other, indicating that this storm produced large hail for much of its lifetime. However, these values did not extend much below $z = 5$ km until 2200 UTC (16 min prior to the plowable hail report), when a column of negative Z_{DR} and small ρ_{HV} descended toward the surface (arrow in Figs. 15a and 16a), reaching the lowest height sampled by the radar at 2215 UTC. A peak in K_{DP} occurred ~15 min prior to the

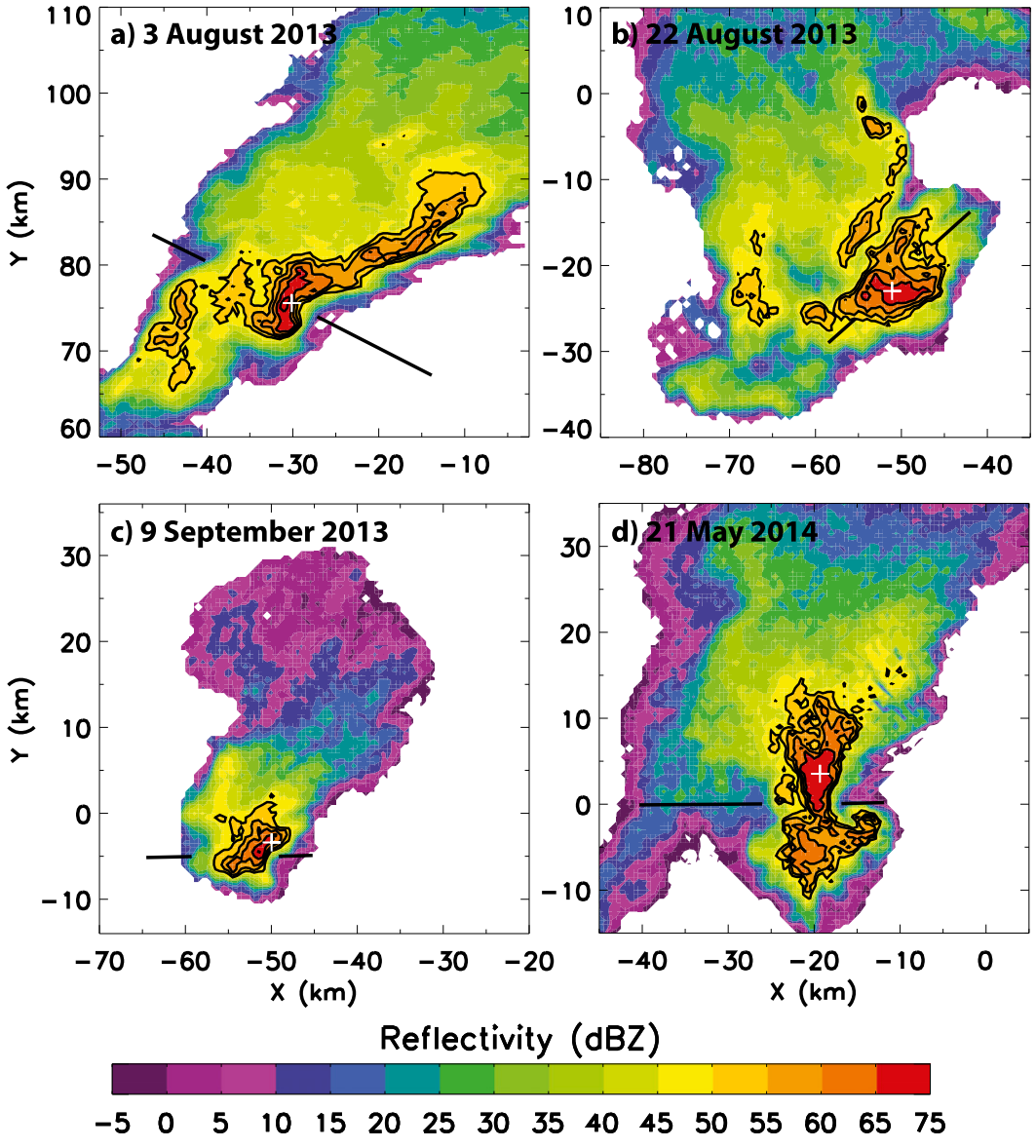

FIG. 9. CAPPIs of reflectivity at (a) 2216 UTC 3 Aug 2013 at z = 3.5 km MSL, (b) 2344 UTC 22 Aug 2013 at z = 3 km MSL, (c) 2107 UTC 9 Sep 2013 at z = 2.5 km MSL, and (d) 2028 UTC 21 May 2014 at z = 2.5 km MSL. The black contours delineate reflectivity from 50 to 70 dBZ at intervals of 5 dBZ. The white plus signs indicate the locations of the plowable hail reports. Black lines show the approximate locations of the cross sections in Fig. 13.

plowable hail report (Fig. 17a). Then, K_{DP} decreased as hail production was maximized, which may indicate that the liquid water was accreted onto the hail and subsequently became depleted.

(ii) 22 August 2013 multicell thunderstorm

The 22 August case is unique among the four examined herein because it was the only multicell thunderstorm and the only plowable hail event that was at least partly initiated by an outflow boundary. At ~2315 UTC, a multicell storm cluster that had moved off the foothills encountered an outflow boundary produced by convection farther to the east (Fig. 18a). The interaction resulted in the rapid development of a new convective cell along the eastern flank of the parent thunderstorm (Figs. 18b–d), with the first echoes appearing in the midlevels (6–12 km) at 2320 UTC (Fig. 13e). The new cell rapidly intensified, and maximum column $Z >$ 70 dBZ (Figs. 13g and 14b), near-surface $Z >$ 65 dBZ (Fig. 9b), and accumulating hail all occurred within 20 min of the first echoes from the new cell. The formation of d = 5 mm hailstone embryos (i.e., small frozen

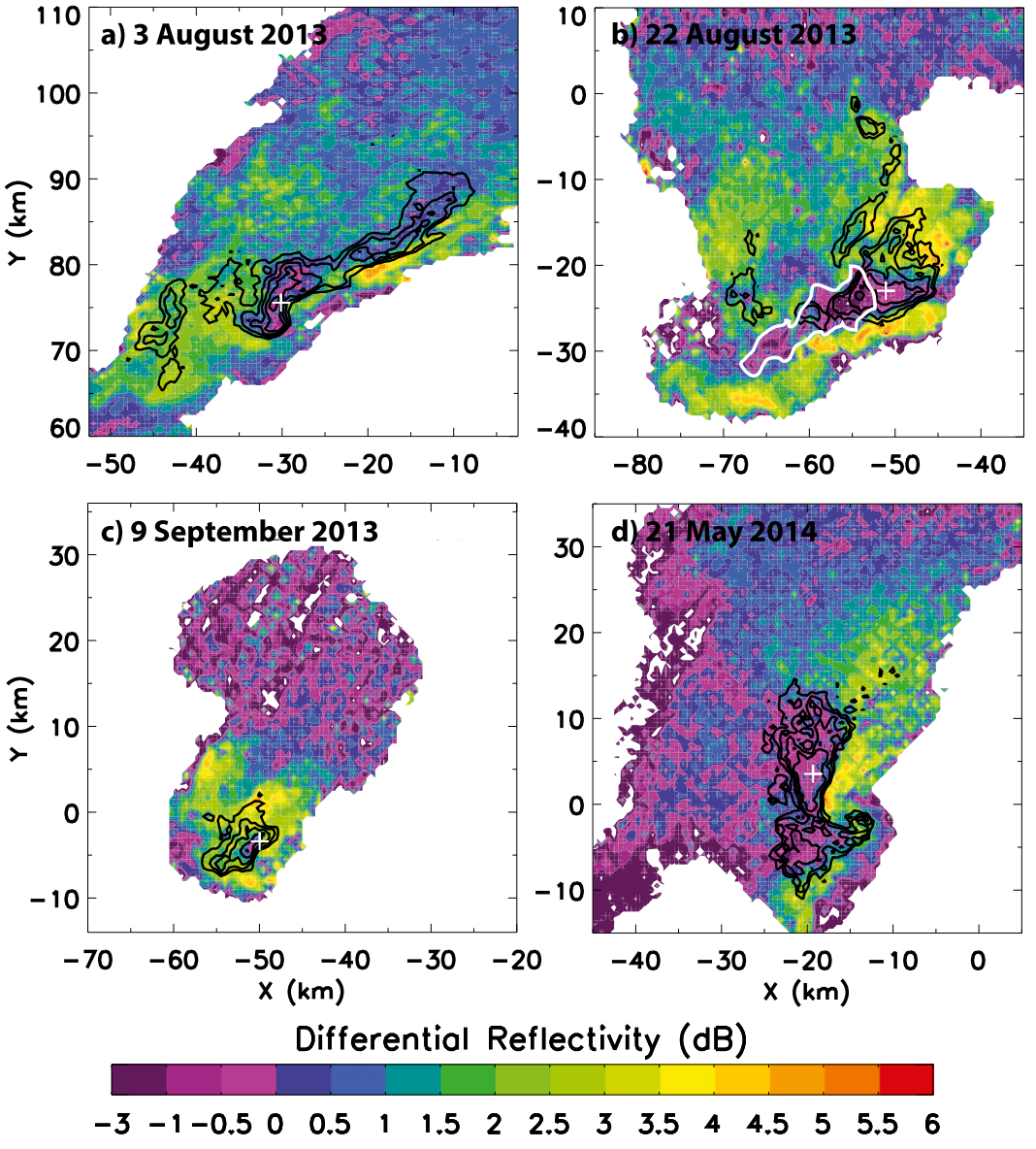

FIG. 10. As in Fig. 9, but for differential reflectivity. The white outline in Fig. 10b indicates an area of negative Z_{DR} discussed in the text.

raindrops or graupel) typically requires 20–30 min, with additional time (~10–20 min) needed to grow embryos into large hail of $d = 45$ mm (Knight and Knight 2001). To achieve such large hail in a total of only 20 min, the hailstone embryos may have grown in the upwind parent thunderstorm, which then seeded the new convective cell with embryos and quickened the hail formation process (documented previously by Ziegler et al. 1983). Unlike the three supercell thunderstorms, vertical cross sections of Z (Figs. 13e–h) provide no evidence of WERs or BWERs, and instead depict an intense core of $Z > 65$ dBZ that rapidly descended to the surface. This further suggests that the mechanism of hail formation (embryo seeding versus embryo recycling) was different in the 22 August storm.

Once hail reached the surface, Z_{DR} and ρ_{HV} CAPPIs depicted minimum values from 0 to −3 dB (Fig. 10b) and 0.85 to 0.95 (Fig. 11b), respectively, within the maximum reflectivity region (black contours). The unusually small Z_{DR} of −3 dB stretched radially behind the region of maximum Z (Fig. 10b, white outline). This feature is evidence of three-body scattering (TBS; Zrnić 1987; Hubbert and Bringi 2000; Kumjian et al. 2010), which occurs when energy from the radar beam is

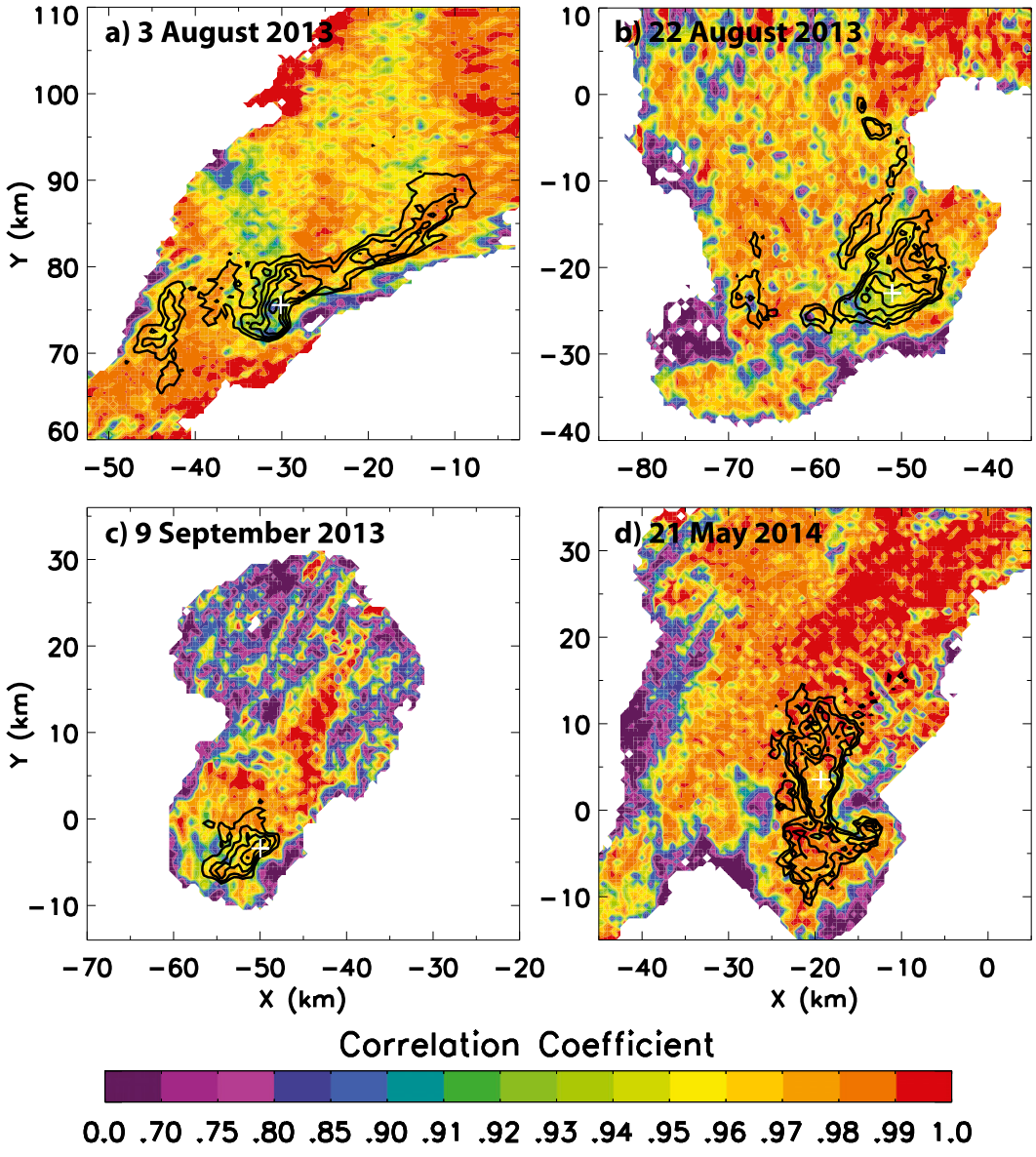

FIG. 11. As in Fig. 9, but for the correlation coefficient.

scattered by hail to the ground, which then scatters the energy back to the hail and finally to the radar. Kumjian et al. (2010) suggested that TBS of the S-band radar beam is indicative of hailstones with $20 \leq d \leq 50.8$ mm, since this signature is not seen in storms that contain mostly small hail ($d < 20$ mm) or predicted from scattering calculations with exclusively giant hail ($d > 50.8$ mm). Since a large amount of hail with $20 \leq d \leq 50.8$ mm is likely to produce the strongest TBS signature, storms that exhibit these signatures on days in which the synoptic environment favors accumulating hail may contain severe hail and have the potential to produce plowable hail.

At the time of the hail reports (2339 UTC), time–height plots of the dual-polarization radar variables clearly indicated the presence of large quantities of hail. Reports of hail coincided with minimum Z_{DR} and ρ_{HV} of -4 dB (Fig. 15b) and 0.45 (Fig. 16b) at $z = 2.5$ km, respectively. These small near-surface values were associated with a column of negative Z_{DR} (from 0 to -2 dB) and small ρ_{HV} (0.75–0.95) that extended to $z = 9$ km, but was most evident at $z < 4$ km where the largest hailstones were likely located. The increased hail production was also accompanied by a decrease in K_{DP} to less than 1° km^{-1} from 3 to 5 km, after K_{DP} peaked at ~2320 UTC (Fig. 17b). The K_{DP} values at the surface

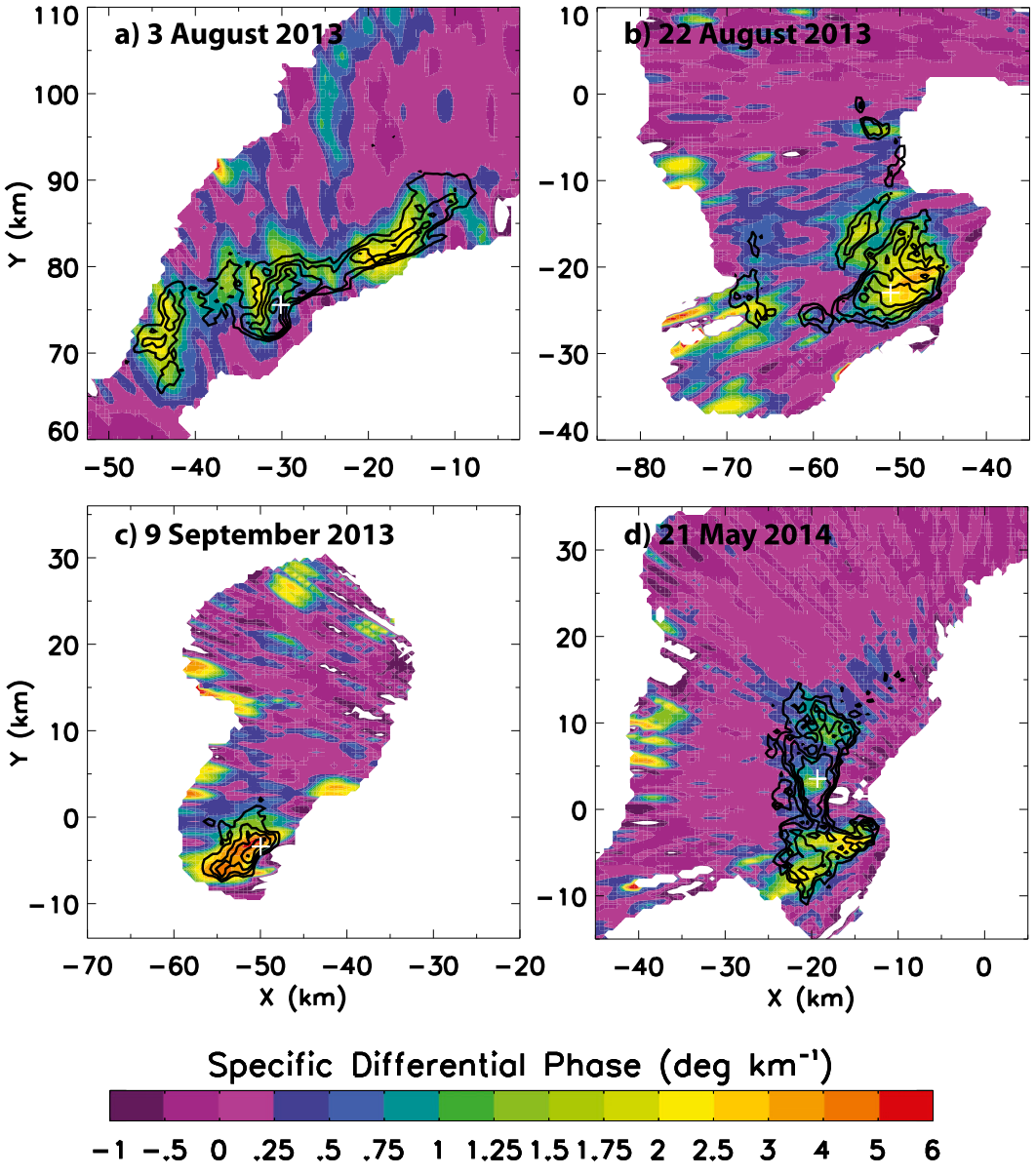

FIG. 12. As in Fig. 9, but for the specific differential phase.

during the hailstorm ranged from 1.5° to 4° km^{-1} (Fig. 12b), indicative of rain mixed with large hail and/or water-coated hail, since K_{DP} is zero for dry, spherical hailstones and increases when liquid water is present (Balakrishnan and Zrnić 1990a).

(iii) 9 September 2013 supercell thunderstorm

On 9 September, a supercell that moved northeastward off the foothills produced plowable hail in Lakewood, Colorado, a western suburb of Denver (Table 1; Fig. 2b). From 2052 to 2106 UTC, vertical cross sections (Figs. 13i–k) and time–height plots (Fig. 14c) of Z depict an intensifying storm. At 2057 UTC, a WER formed (Fig. 13i, black square), which evolved into a BWER at $z = 6.5$ km by 2106 UTC (Fig. 13k). The formation of the WER/BWER occurred as hail accumulated at the surface (2100 UTC). Following the hail report, the BWER descended in height (from $z = 6.5$ to 4 km) and began to collapse as rain and hail descended through the updraft (2116 UTC; Fig. 13l).

The 9 September storm contained the smallest hail ($d \leq 13$ mm) out of the four cases (Table 1). The small hailstones contributed to $Z > 70$ dBZ (Fig. 9c), with Z_{DR} from −0.25 to 3 dB (Fig. 10c). These values imply

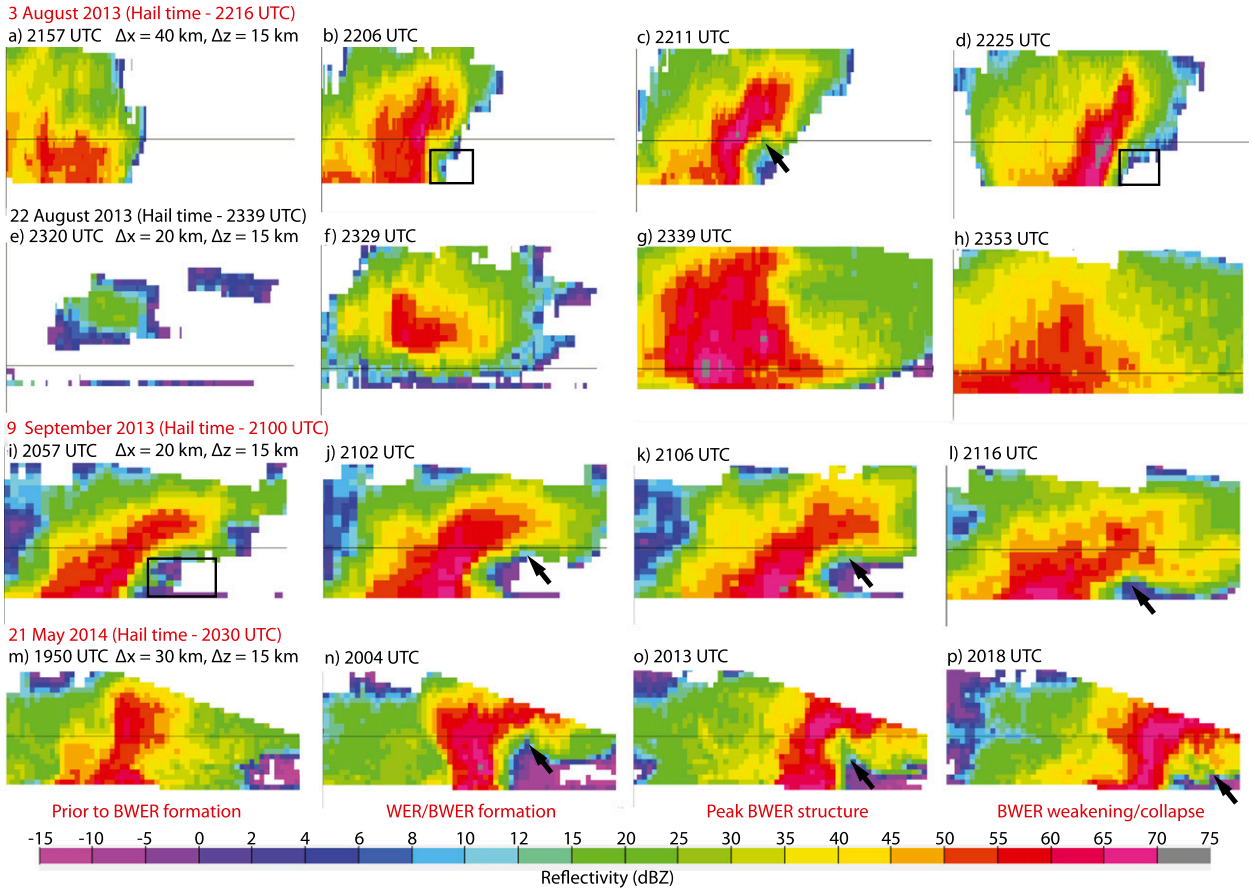

FIG. 13. Vertical cross sections of reflectivity along the lines shown in Fig. 9 at (a)–(d) 3 Aug 2013, (e)–(h) 22 Aug 2013, (i)–(l) 9 Sep 2013, and (m)–(p) 21 May 2014 at the indicated times. Black squares (arrows) show the locations of WERs (BWERs). The red labels at the bottom of each column apply to the dates indicated in red (i.e., 3 Aug 2013, 9 Sep 2013, and 21 May 2014). Here, Δx and Δz are the total length and height of the cross sections in each row, respectively.

melting hail coated with liquid water, causing the hailstones to appear more oblate (i.e., more similar to rain) to the radar than the hail in the other three storms. There is no evidence of TBS (Fig. 10c), in accordance with Kumjian et al. (2010), who suggested that hail of $20 \leq d \leq 50$ mm is required to produce TBS. The presence of $\rho_{HV} \sim 0.95$ (Fig. 11c) and K_{DP} of up to $6° \text{ km}^{-1}$ (Fig. 12c) suggests that a large amount of rain was mixed with the water-coated hailstones.

In general, trends in the time–height cross sections on 9 September (Figs. 14c–17c) do not show as distinct of a hail signature as in the other cases, possibly because of the small sizes of the hailstones ($d \leq 13$ mm; Table 1) and the heavy rainfall that accompanied them. While the maximum column Z of ~72 dBZ (denoted as 2 in Fig. 14c) occurred in conjunction with the hail report, there was little increase in 50-dBZ echo-top height. The storm also produced limited graupel and hail mass surrounding the plowable hail report ($<3 \times 10^7$ kg; Fig. 14c), likely because of the small size of its maximum reflectivity region (Fig. 9c). The smallest values of Z_{DR} (Fig. 15c) and ρ_{HV} (Fig. 16c) below $z = 3$ km occurred at 2030 UTC, 30 min before the hail report when the storm was still over the foothills (Fig. 2a). Once hail began to accumulate at the surface at 2100 UTC, minimum Z_{DR} (ρ_{HV}) values had increased by about 1 dB (0.3) at $z =$ 2.5 km, likely because of the presence of water-coated hailstones (inferred from $K_{DP} > 3° \text{ km}^{-1}$; Figs. 12c and 17c).

(iv) 21 May 2014 supercell thunderstorm

The final storm discussed herein is a tornadic supercell that produced five separate tornadoes to the east of Denver and accumulating hail in Green Valley Ranch, Colorado (Table 1; Fig. 2b). A time–height plot of Z (Fig. 14d) depicts maxima in 50-dBZ echo-top height of ~12 km and maximum column $Z > 70$ dBZ (denoted as 1 in Fig. 14d) about 30 min prior to the plowable hail

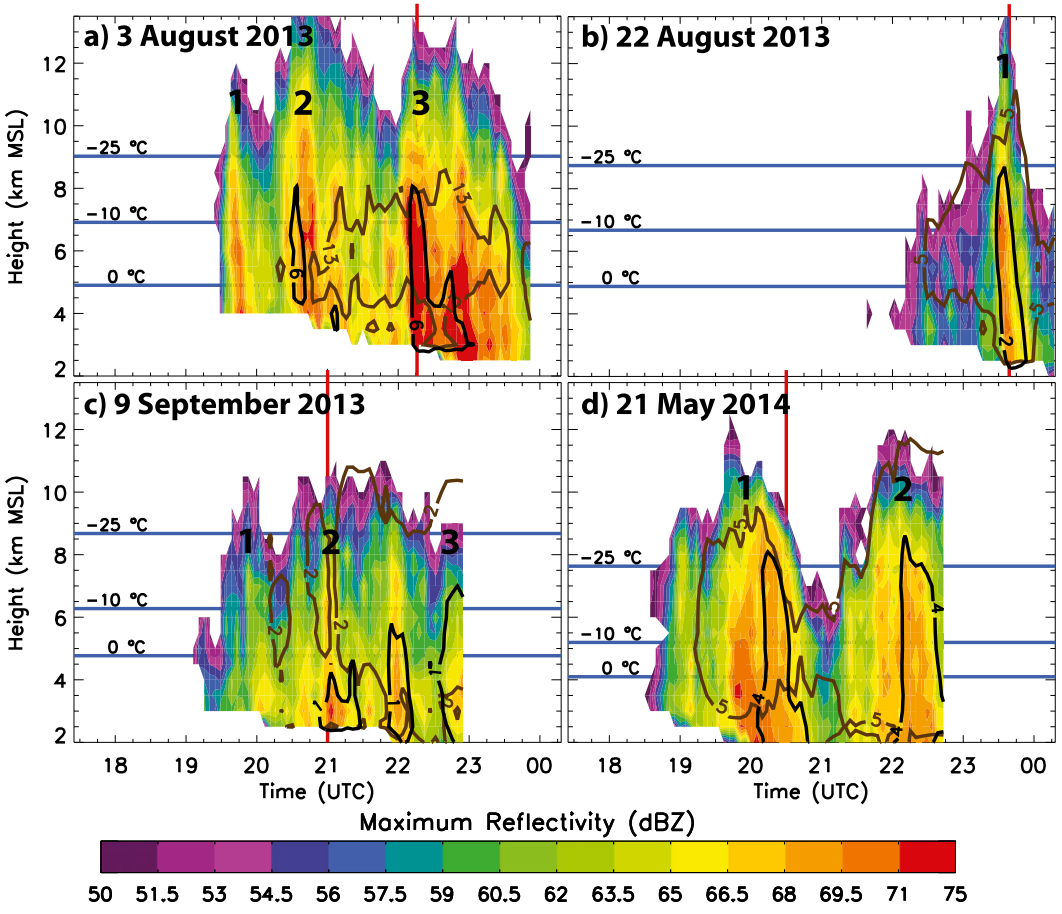

FIG. 14. Time–height plots of the maximum reflectivity for $Z \geq 50$ dBZ for the hailstorms on (a) 3 Aug 2013, (b) 22 Aug 2013, (c) 9 Sep 2013, and (d) 21 May 2014. Brown (black) contours indicate areas and times of enhanced graupel (hail) production ($\times 10^7$ kg). The red vertical lines in the background depict the times that plowable hail was reported. The blue horizontal lines depict the heights of the 0°, −10°, and −25°C isotherms from the operational soundings listed in Table 2. The black numbers (1–3) in boldface indicate maxima in 50-dBZ echo-top height and column reflectivity.

report at 2030 UTC. Similar to the two supercell thunderstorms examined earlier, vertical cross sections of Z reveal that these maxima were associated with a pronounced BWER that formed by 2004 UTC (Fig. 13n) and persisted through 2013 UTC (Fig. 13o). By 2018 UTC (Fig. 13p), the BWER had clearly begun to collapse and descend toward the surface. This collapse occurred at the same time that hail mass peaked at $>4 \times 10^7$ kg (Fig. 14d) and ~12 min before accumulating hail was reported. This suggests that the BWER collapse may have been caused by hail mass overloading the updraft. In agreement with this hypothesis, Z weakened by ~10 dB throughout the column in the 30 min that followed the hail report. This weakening began shortly after the peak radar-derived hail mass was observed, whose downward mass flux would have reduced the local buoyancy through sedimentation-induced drag and latent cooling from melting and sublimation (Srivastava 1987; Lee et al. 1992; Zeng et al. 2001).

Similar to the previous hailstorms, the 21 May storm also had near-surface $Z > 65$ dBZ (Fig. 9d). A prominent hook echo is also evident. Near-surface Z_{DR} and ρ_{HV} reached minimum values of −1 dB (Fig. 10d) and 0.95 (Fig. 11d), which are not as small as in the August 2013 hailstorms. This is likely due to the smaller maximum hail diameter in this storm (25 versus 45 mm). Nevertheless, TBS is still apparent, with a widespread area of negative Z_{DR} located radially behind the area of maximum Z (Fig. 10d). This storm also contained near-surface K_{DP} values of 0–2° km^{-1} (Fig. 12d), indicative of relatively small raindrop concentrations.

In the vertical (Figs. 15d–17d), a pocket of $Z_{DR} \sim -2$ dB and $\rho_{HV} \sim 0.8$ formed near $z = 5$ km at 1935 UTC and reached the lowest radar level ($z = 2$ km) at

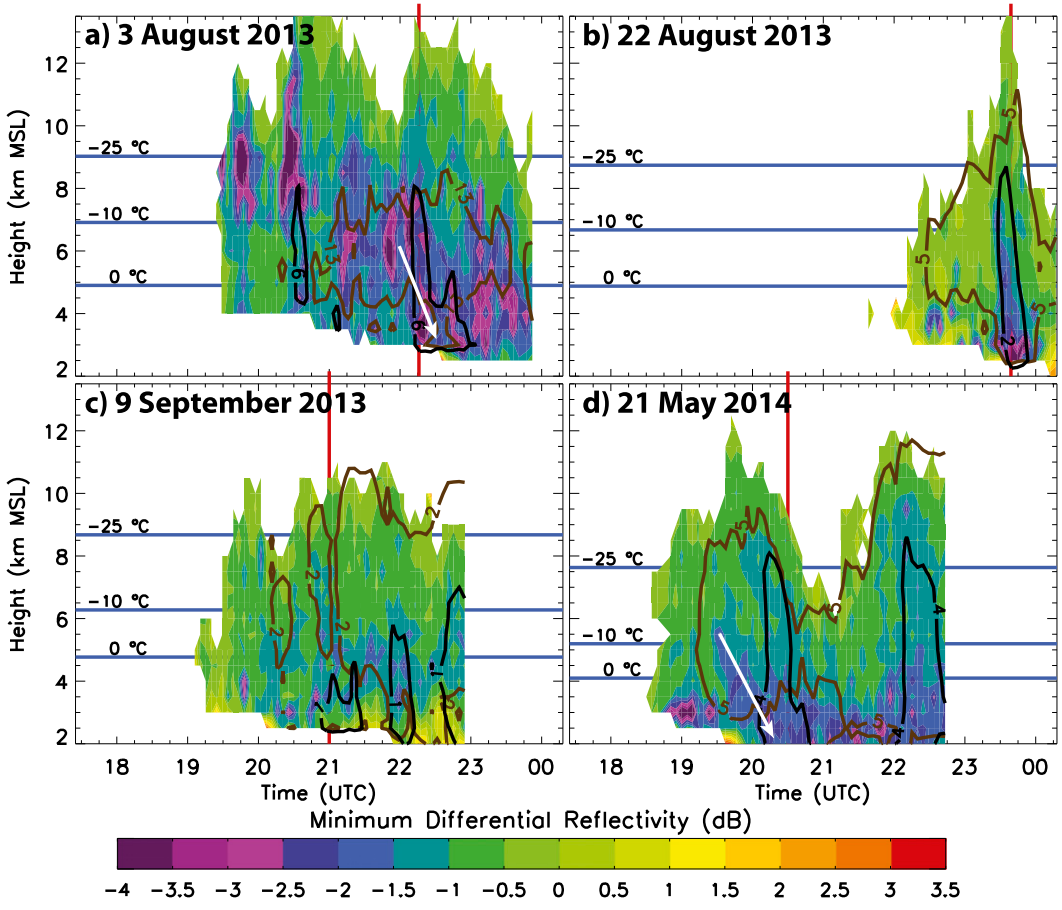

FIG. 15. As in Fig. 14, but for the minimum differential reflectivity. The arrows indicate descending areas of small Z_{DR}.

2015 UTC (15 min prior to the plowable hail report; arrow in Figs. 15d and 16d). The descent of the small Z_{DR} and ρ_{HV} values was generally less pronounced on 21 May than during the August 2013 hailstorms, which had larger hail and minimum Z_{DR} and ρ_{HV} values of −4 dB and 0.4, respectively. No peak in K_{DP} occurred prior to the plowable hail report on this day (Fig. 17d).

2) ESTIMATING HAIL ACCUMULATION FROM RADAR DATA

The radar characteristics discussed thus far are not exclusive to thunderstorms that produce deep hail accumulations. Although rather extreme, $Z > 70$ dBZ, descending columns of negative Z_{DR} and $\rho_{HV} < 0.95$, and TBS signatures have all been observed in non-accumulating hailstorms (e.g., Hubbert and Bringi 2000; Kumjian and Ryzhkov 2008; Ryzhkov et al. 2010). To identify the occurrence of plowable hail in real time, we propose that forecasters estimate the hail accumulation hAcc from the radar data:

$$\mathrm{hAcc} = \frac{v}{\eta \rho_h} \sum_{t=t_0}^{t_{\mathrm{current}}} \Delta t_t M_{h,t}, \tag{4}$$

where M_h is the hail mass concentration [kg m^{-3}; determined from Eq. (2) and the method discussed in section 3b] at the lowest radar level, Δt is the time (s) between successive radar scans, v is the hail fall speed (cm s^{-1}), ρ_h is the hail bulk density (kg m^{-3}), and η is the fractional space occupied by ice (rather than air) once the hailstones accumulate on the ground. We have assumed $v = 1500$ cm s^{-1} [appropriate for a $d = 20$ mm hailstone; Pruppacher and Klett (1997)], $\rho_h = 900$ kg m^{-3}, and $\eta = 0.64$, the closest possible random packing of monodisperse spheres (Scott and Kilgour 1969). For each radar grid cell, the product $\Delta t M_h$ can be computed for all radar scans since the formation of the hailstorm (t_0) to the current time (t_{current}) and then summed to map the storm-total hail accumulation. In this way, Eq. (4) is similar to existing operational, radar-based algorithms that use time-integrated rainfall rates

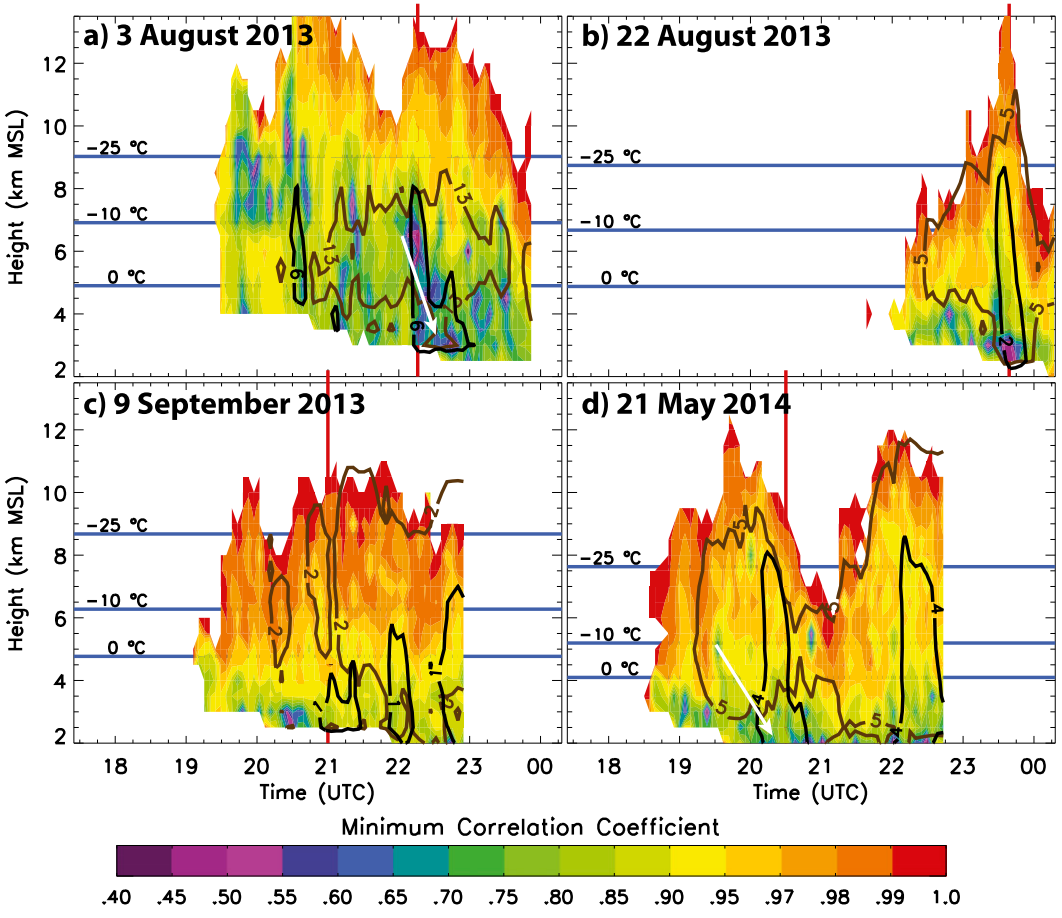

FIG. 16. As in Fig. 14, but for the minimum correlation coefficient. The arrows indicate descending areas of small ρ_{HV}.

R from Z–R or K_{DP}–R relationships (e.g., Marshall and Palmer 1948; Rosenfeld et al. 1993; Bringi and Chandrasekar 2001; Illingworth and Blackman 2002; Brandes et al. 2002) to estimate storm-total rainfall and to assess the risk of flash flooding.

The results of applying this procedure to the radar scans within the analysis periods in Table 1 are shown in Fig. 19. In all four cases, the plowable hail reports (black squares in Fig. 19) are collocated with hAcc $>$ 5 cm, whereas the remainder of each hail swath mostly contains hAcc $<$ 1.5 cm. Two exceptions (circled areas) occur on 3 August (Fig. 19a) and 21 May (Fig. 19d), when hAcc near 10 cm is noted well to the northwest and east of the hail reports, respectively. The area on 3 August is an unpopulated region of the foothills to the south of the Wyoming border (Fig. 2), and thus it cannot be determined whether the estimated hail accumulations actually occurred. While the circled area in Fig. 19d is also sparsely populated, storm chasers reported and photographed hail accumulations of at least 10 cm in this area in the wake of the 21 May hailstorm. These results suggest that the above technique is capable of distinguishing between times and locations at which accumulating hail does and does not occur. However, additional plowable hail events need to be examined to evaluate the algorithm more completely.

3) HAIL SIZE

One might assume that as hail size increases, the hail number concentration must decrease because a greater fraction of the total liquid water content is accreted onto each hailstone. Therefore, it may be expected that plowable hailstorms consist primarily of small hail particles ($d < 25.4$ mm). While the hail sizes listed in Table 1 suggest otherwise, one could argue that because these sparse reports consist of the maximum hail size documented anywhere within the storm near the time of plowable hail, they are unlikely to represent the hail size at the accumulation location. Since hail size observations from the accumulations are not available, we must use the dual-polarization radar data in our attempt to quantify the hail sizes in these events.

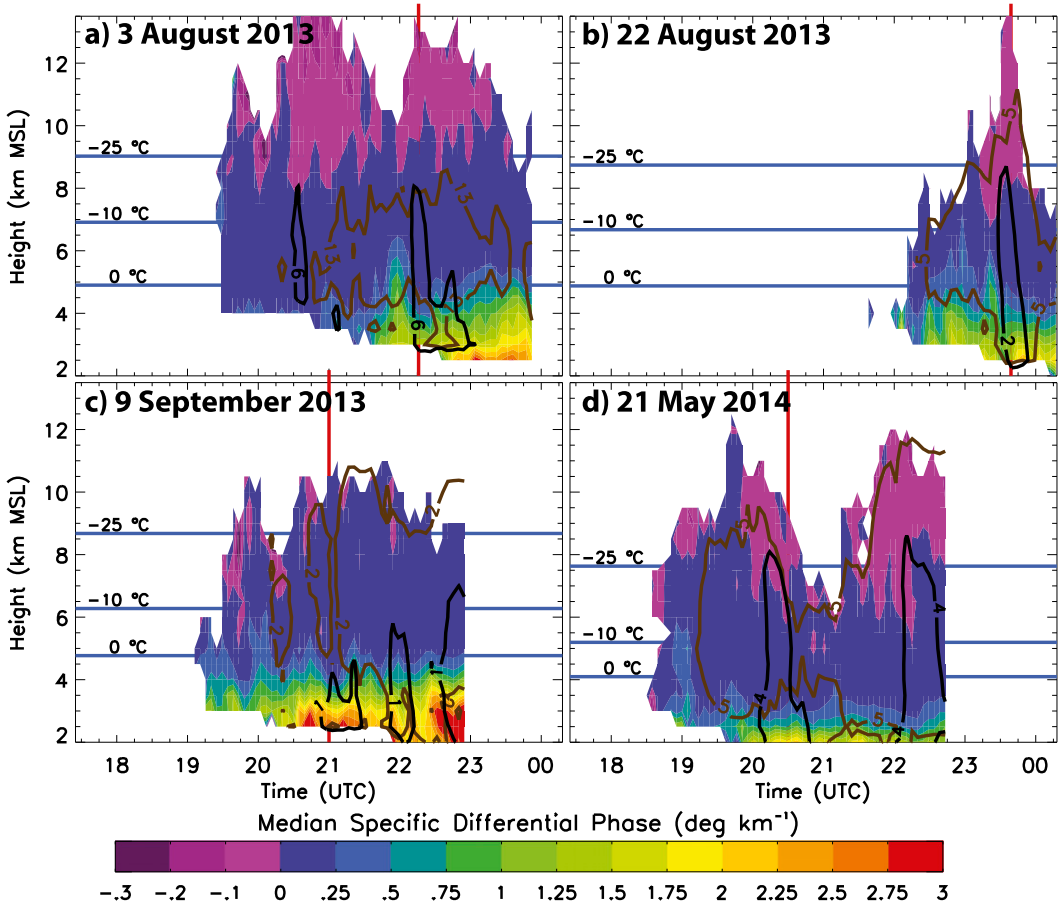

FIG. 17. As in Fig. 14, but for the median specific differential phase.

Aydin et al. (1986) defined the hail differential reflectivity H_{DR}, which uses radar-measured Z and Z_{DR} to quantify the hail signal intensity [see their Eq. (1)]. Depue et al. (2007) showed that H_{DR} was well correlated ($r^2 = 0.54$) with observed hail size in 12 Colorado and Wyoming thunderstorms, with $H_{DR} \sim 30$ dB indicative of the threshold for large hail ($d = 25.4$ mm; their Fig. 5). Figure 20 presents time series of H_{DR} at the lowest available radar height in the four hailstorms considered herein, including median H_{DR} (blue line), maximum H_{DR} (red line), and H_{DR} at the plowable hail location (orange squares). Over the time intervals in which hail occurred at the plowable hail locations, H_{DR} generally ranged from the median H_{DR} to the maximum H_{DR} observed in the storms. This suggests that the larger hailstones contained within the storms are at least present in the hail accumulations, if not the dominant contributors to them. Figure 20 also shows that except during the 3 August storm, the maximum H_{DR} within the storm occurred at the plowable hail location for at least one radar volume scan. If we assume that the maximum H_{DR} represents the hail diameters reported in Table 1, then large hail ($d > 25.4$ mm) occurred at the plowable hail locations in all of the storms except the 9 September event, which contained no large hail.

Since Z and Z_{DR} (and thus H_{DR}) are heavily biased toward the largest particles in the radar volume, we still cannot quantify the median hail sizes contained within the accumulations. Further, T-matrix scattering simulations demonstrate that H_{DR} is sensitive to the fractional water content of hailstones (Depue et al. 2007), which may be why the H_{DR} analysis implies the presence of large hail in the 9 September storm when none occurred. Given these limitations, it is vitally important for observers of future plowable hailstorms to report maximum and average hail sizes, in addition to hail depths, so that more can be learned about the hail size distribution in these exceptional storms.

c. *Lightning and ice mass analysis*

We now investigate whether three-dimensional total lightning data offer any assistance in identifying

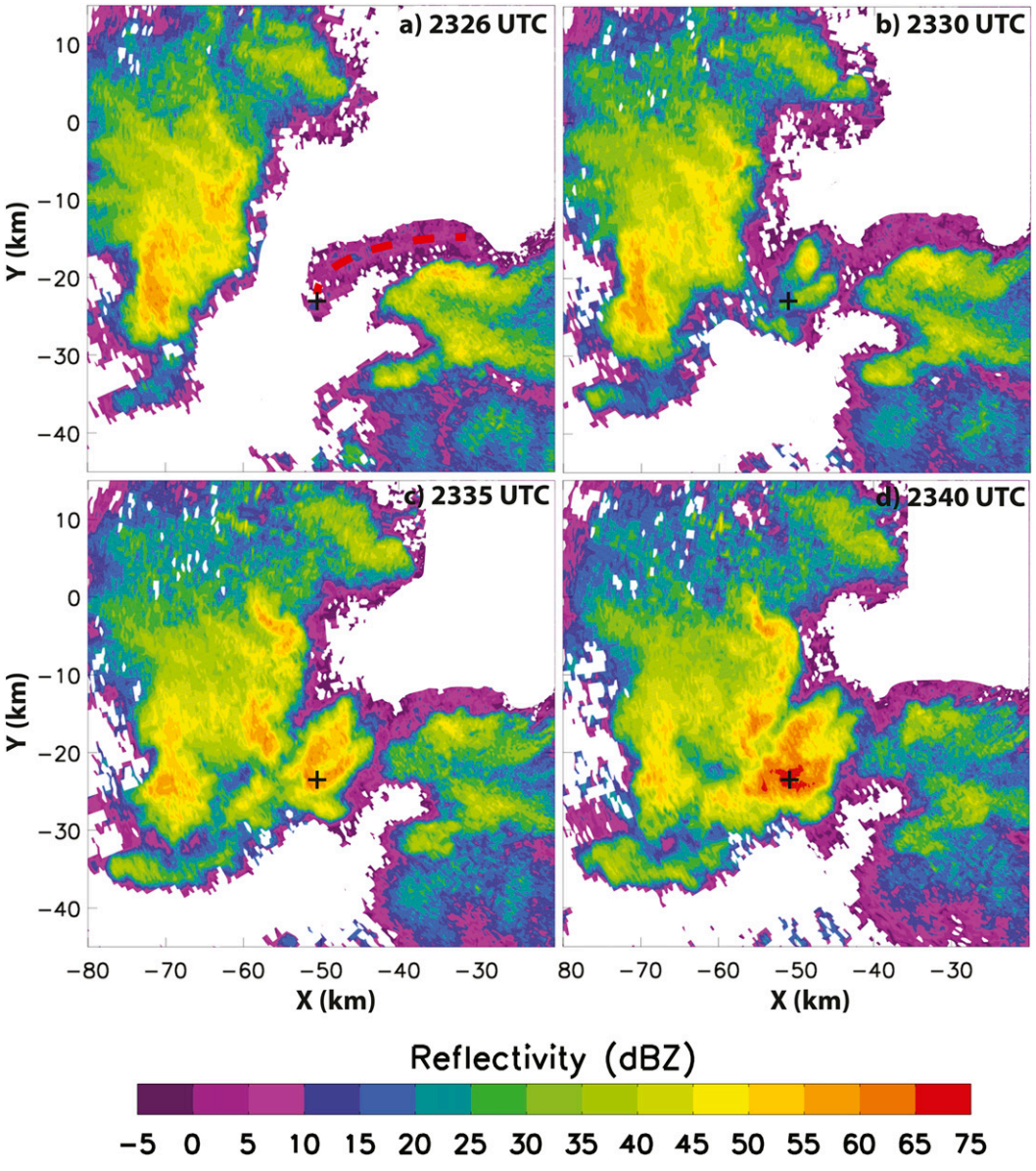

FIG. 18. PPIs of reflectivity at 0.5° elevation angle at (a) 2326, (b) 2330, (c) 2335, and (d) 2340 UTC 22 Aug 2013. The black plus sign indicates the plowable hail location and the red dotted line indicates an outflow boundary.

plowable hail events. Figure 21 presents time series of lightning flash rate (calculated from all flashes produced by the hailstorm; see section 3c) and storm-total graupel mass for the analysis time intervals in Table 1. Note that the COLMA detection efficiency is relatively uniform within 150 km of the array center (P. R. Krehbiel 2015, personal communication), which covers nearly all of the electrically active portions of the storm tracks (Fig. 2). Lightning flash rates at the plowable hail report times (denoted by dashed black lines) ranged from 25 flashes min^{-1} in the 9 September storm (Fig. 21c) to 260 flashes min^{-1} on 3 August (Fig. 21a), the latter of which was closest to COLMA (Fig. 2). In three of the four storms (the exception being 21 May; Fig. 21d), the flash rates at the plowable hail report times were at or near the largest observed thus far within the storm. Additionally, plowable hail occurred as the flash rate was increasing on 22 August (Fig. 21b) and 21 May (Fig. 21d). On 22 August, flash rates more than doubled in the 30 min prior to the hail report. Although accumulating hail may have occurred at other times (e.g., ~2310 UTC 3 August and ~2145 UTC 21 May) when similar maxima in flash rate occurred, it was not reported, possibly because of the remote location.

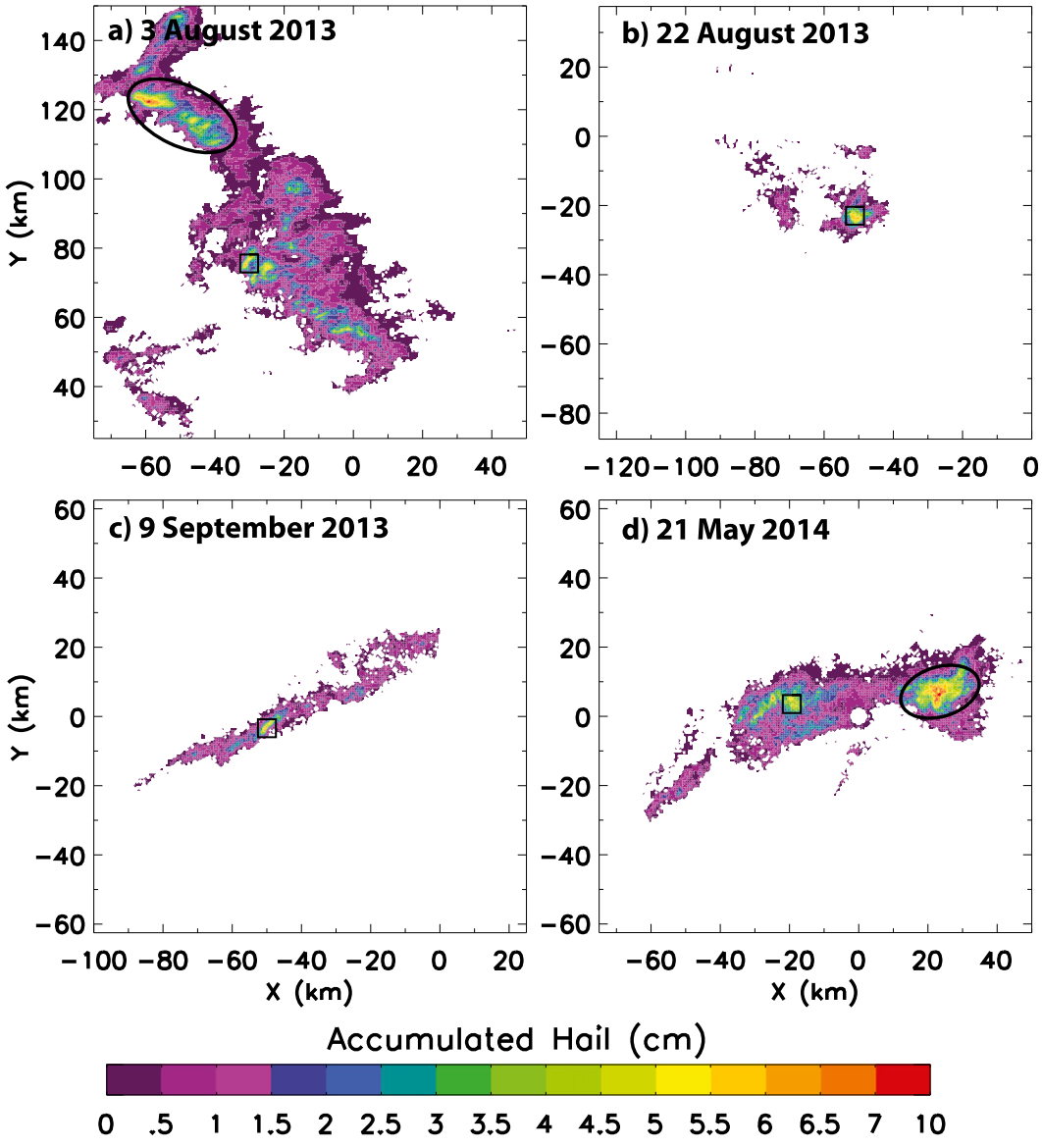

FIG. 19. Accumulated hail depths estimated from the radar data on (a) 3 Aug 2013, (b) 22 Aug 2013, (c) 9 Sep 2013, and (d) 21 May 2014. Squares indicate the locations of the plowable hail reports. Inferred areas of accumulating hail that occurred in sparsely populated locations are circled.

The time series in Fig. 21 demonstrate that the flash rate increases prior to accumulating hail were also accompanied by increases in the storm-total graupel mass (with the period from 2000 to 2045 UTC on 21 May being an exception; Fig. 21d). Overall, it is evident that the flash rates are well correlated with the total graupel mass, similar to the results shown by Carey and Rutledge (1996), Wiens et al. (2005), and Deierling et al. (2008). This correlation r ranges from 0.77 to 0.83 over the analysis period (not shown), which included 35 (22 August 2013) to 68 (21 May 2014) radar volume scans. The graupel mass is also well correlated with other lightning characteristics, such as the maximum observed flash area (not shown; r = 0.64–0.74). Note, however, that the growth in the storm size is a confounding variable that increases both the flash area and the total graupel mass. The relationship between lightning and graupel mass is also apparent when examining maps of the total-column graupel mass and the total number of lightning sources contained in the flashes (Fig. 22). Peaks in the number of lightning sources generally coincide with peaks in the total-column graupel mass, and the largest number of lightning sources in each storm is typically associated with column graupel

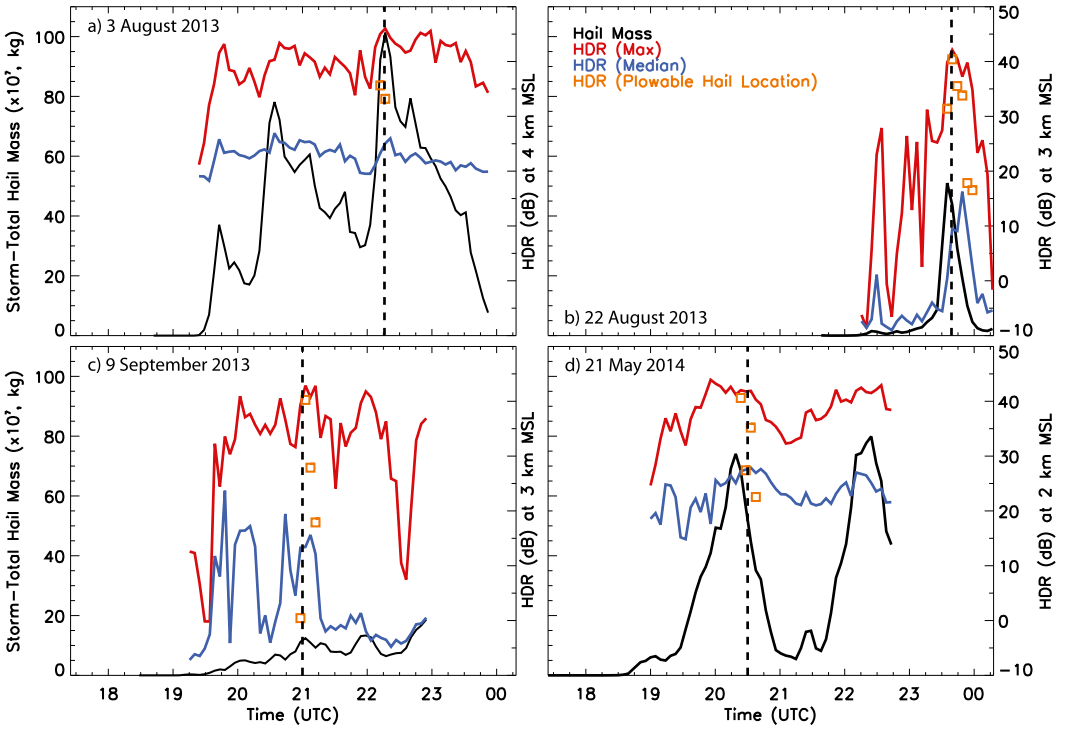

FIG. 20. Time series of storm-total hail mass (black solid lines) and maximum H_{DR} (red lines), median H_{DR} (blue lines), and H_{DR} at the plowable hail locations (orange squares) at the indicated heights on (a) 3 Aug 2013, (b) 22 Aug 2013, (c) 9 Sep 2013, and (d) 21 May 2014. The vertical dashed black lines indicate the plowable hail report times.

masses greater than 10^6 kg. Figure 22 also illustrates that increases in graupel mass and lightning activity occur along the storm track prior to the occurrence of plowable hail.

Storm electrification has been observed to occur when graupel particles undergo rebounding collisions with ice crystals (e.g., Williams et al. 1991; Saunders 1993; Takahashi and Miyawaki 2002; Saunders 2008). The time–height plots of reflectivity and ice mass (Fig. 14) demonstrate that graupel production increases substantially when maxima in echo-top height and reflectivity occur. These maxima are suggestive of intense updrafts that support both graupel and hail formation and cause the lightning flash rate to increase because of the additional graupel mass. While forecasters may not be able to calculate total graupel mass easily, Fig. 21 demonstrates that another quantity, the area of the 40-dBZ isoecho at the approximate height of the −10°C isotherm (determined from atmospheric soundings; Table 2), closely tracks the time series of storm-total graupel mass and can be used as a proxy. It is not surprising that this quantity mirrors the trend in graupel mass, since $Z > 40$ dBZ at −10°C likely requires the existence of graupel and/or hail at this height. The presence of 40-dBZ reflectivity at the −10°C isotherm height has also been successfully used to predict the onset of lightning (e.g., Dye et al. 1989; Gremillion and Orville 1999; Vincent et al. 2003), a further indication of its relationship to graupel mass. Therefore, forecasters can use either the area of the 40-dBZ isoecho at −10°C or the total lightning flash rate (or both) to indirectly estimate the graupel mass and the intensity of the thunderstorm updraft, thereby providing insight into whether hail accumulations (and other hazardous weather events) are possible.

In addition to the relationship with graupel mass, time series of lightning flash rate (red lines in Fig. 23) and 50-dBZ echo-top height (blue lines in Fig. 23) reveal that increases (decreases) in lightning flash rate were generally accompanied by corresponding increases (decreases) in echo-top height. Two notable exceptions to this relationship (denoted by green lines along the x axes) occurred on 3 August (Fig. 23a) and 21 May (Fig. 23d), when decreases in echo-top height of ~5 km were accompanied by dramatic increases in lightning flash rate of 1100% and 150%, respectively. These changes occurred over the course of ~1 h in both cases, and the increases (decreases) in lightning flash rate (echo-top height) on 21 May coincided with the plowable hail report and the collapse of a pronounced

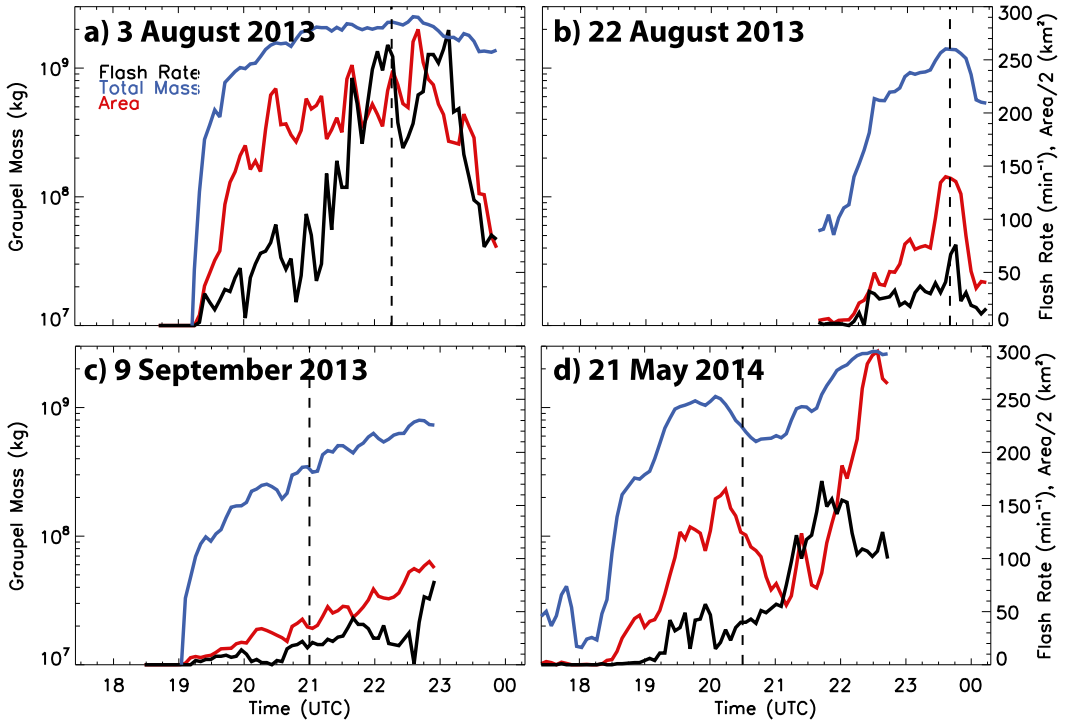

FIG. 21. Time series of storm total graupel mass (blue lines), lightning flash rate (black solid lines), and the area of the 40-dBZ isoecho at the approximate height of the −10°C isotherm (red lines) for the hailstorms on (a) 3 Aug 2013, (b) 22 Aug 2013, (c) 9 Sep 2013, and (d) 21 May 2014. The dashed black lines indicate the times that plowable hail was reported.

BWER (Figs. 13o–p). Increases in lightning flash rate accompanying storm collapse have been observed previously (e.g., Carey and Rutledge 1998; Shafer et al. 2000; Wiens et al. 2005). These studies reported that lightning flash rate peaked tens of minutes after hailfall in these storms, as was the case on 21 May. It is hypothesized that in these cases, the collapse of the storm increased the number of rebounding collisions between graupel and ice crystals and caused pockets of opposite charge to become adjacent to one another, thereby explaining the observed increases in flash rate. Notably, there is no obvious relationship between the height of the maximum number of lightning sources summed over all of the flashes and the flash rates or storm life cycle (black lines in Fig. 23) in the cases examined herein.

5. Discussion

Section 4 revealed that accumulating hail is associated with some of the more extreme values of the radar signatures (i.e., $Z > 70$ dBZ, $Z_{DR} \sim -3$ dB with extensive three-body scattering, $\rho_{HV} \sim 0.4$, and well-defined BWERs) typically associated with hailstorms, especially since giant hail was not documented in these storms. Nevertheless, the four plowable hailstorms examined herein are typical hailstorms except for one (or possibly two) brief periods of time. We know this because ground observations of hail along the storm tracks and radar-derived indicators of hail, such as those shown in Figs. 19 and 20, confirm that these thunderstorms produced hail for much of their lifetimes. Only a small fraction of this hail, however, was reported to be plowable.

The hail accumulation at a particular location depends on the hail mass concentration and the hailfall duration (related to the storm propagation speed), as reflected by Eq. (4). Thus, plowable hail events must be associated with unusually long hailfall durations, unusually large hail mass concentrations, or a combination of these. The radar-derived hailfall durations at the plowable hail locations were 9.3 min on 3 August, 18.6 min on 9 September and 21 May, and 28.0 min on 22 August (time period denoted by orange squares in Fig. 20). These durations are near the 50th, 80th, and 95th percentiles of the cumulative frequency distribution of hailfall duration calculated from a sample of 2524 hail events in southern France (Dessens 1986, their Fig. 10). Changnon (1967) reported monthly average hail durations that ranged from 1.4 to 3.2 min in

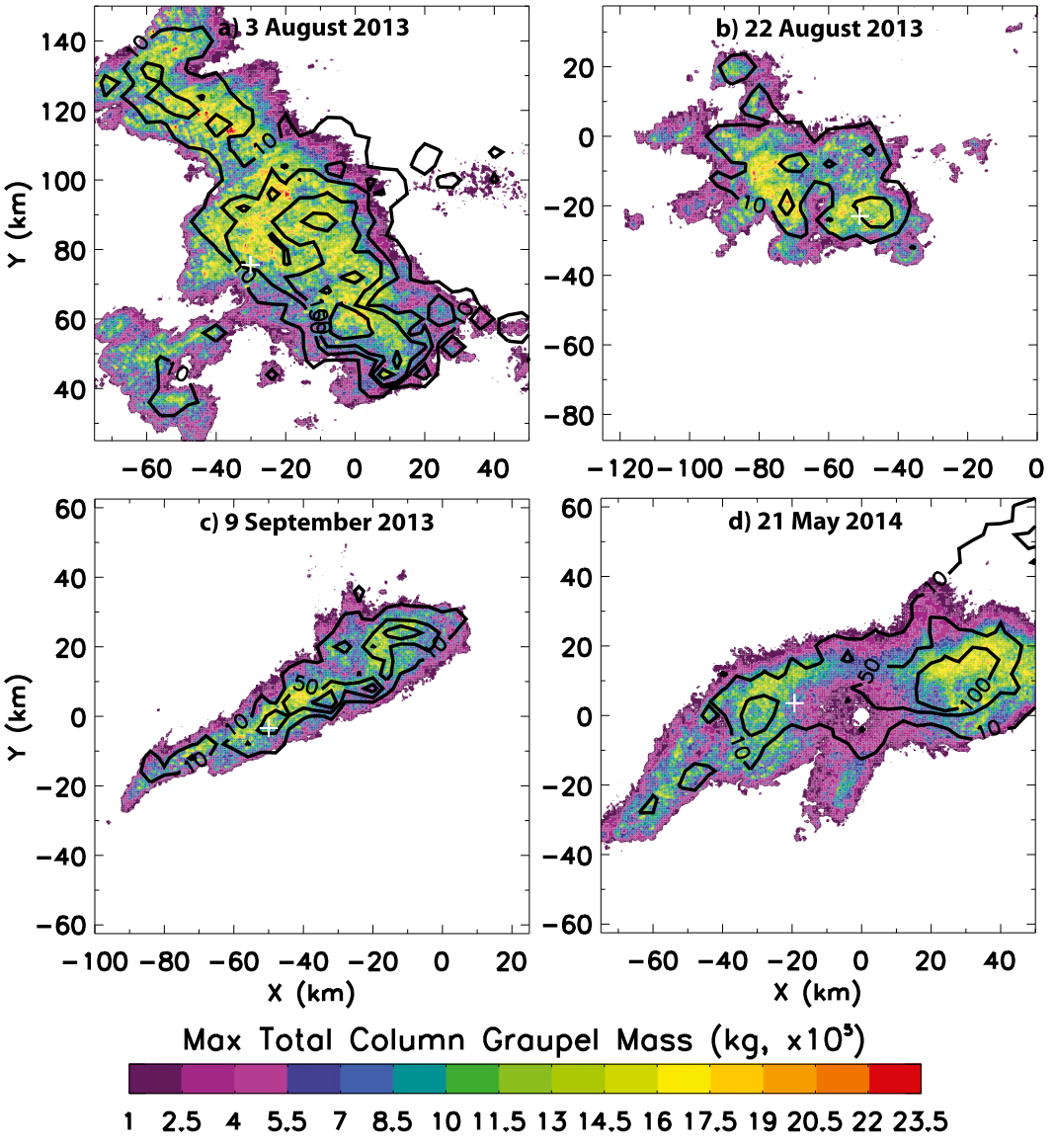

FIG. 22. Maximum total-column graupel mass (filled contours) and number of lightning sources summed over all lightning flashes (black contours with values of 10, 50, 100, 250, and 500) on (a) 3 Aug 2013, (b) 22 Aug 2013, (c) 9 Sept 2013, and (d) 21 May 2014. White plus signs indicate the locations of the plowable hail reports.

99 hailstorms in Illinois, which would make even the 3 August event (9.3 min) long by comparison. Other median hailfall durations reported in the literature include 5–6 min [Saskatchewan, Canada; Paul (1980)] and 7 min [Alberta, Canada; Wojtiw (1975)]. Thus, it is likely that the long hailfall durations (9–28 min) in these four plowable hail events, made possible by slow storm motions of 6–9 m s^{-1} (Table 1), are a characteristic that distinguishes them from more typical hail events.

It is more difficult to quantify how anomalous the hail mass concentration is in these storms, because the best available estimate of the mass concentration is based solely on the radar reflectivity [Eq. (2)]. We have already noted that maximum Z values of 68–75 dBZ are on the larger end of the spectrum that characterizes typical hailstorms. If these values are indeed proportional to the mass concentration, then the above discussion suggests that plowable hail events result from unusually long hailfall durations that consist of larger than normal hail concentrations. These factors are similar to those required for flash flooding, which results from a combination of rainfall duration and rain rate, and explain why similar equations [i.e., Eq. (4)] can be used to identify these events in real time.

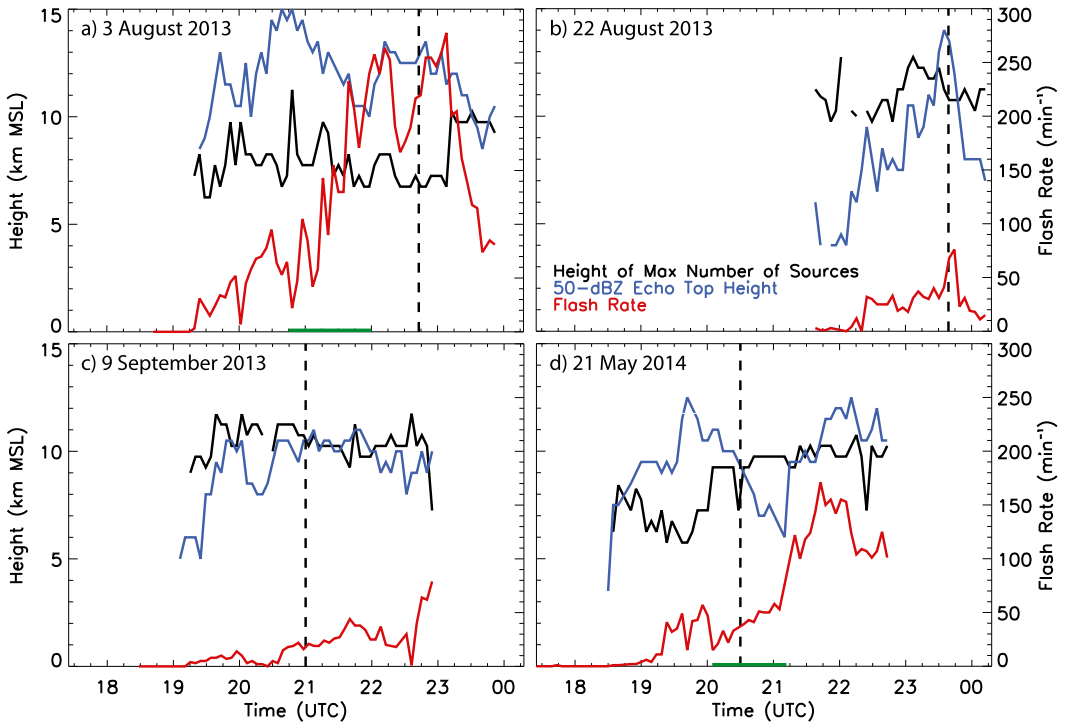

FIG. 23. Time series of the height of the maximum number of sources summed over all lightning flashes (black lines), the 50-dBZ echo-top height (blue lines), and the lightning flash rate (red lines) on (a) 3 Aug 2013, (b) 22 Aug 2013, (c) 9 Sep 2013, and (d) 21 May 2014. The green lines along the x axes indicate time intervals when the echo-top heights and the lightning flash rates were decreasing and increasing, respectively. The vertical dashed black lines indicate the plowable hail report times.

Another similarity between excessive rainfall and excessive hailfall is that there may not be a unique signature in the raw radar or lightning variables that discriminates between plowable and nonplowable hailstorms (or between flooding and nonflooding rainstorms). This null result is an important one because it demonstrates that hail accumulations must be derived from the radar data to identify these events, just as radar-derived rainfall amounts are needed to determine the likelihood of flash flooding.

6. Summary and conclusions

In this paper, we analyzed dual-polarization radar and total lightning data from four thunderstorms that resulted in hail accumulations of 15–60 cm along the Colorado Front Range during 2013–14 (Table 1; Fig. 2). The synoptic weather conditions that favored the development of these storms were examined in conjunction with radar (Z, Z_{DR}, ρ_{HV}, K_{DP}, H_{DR}, ice mass, and hail depth) and lightning (flash rate) variables that might indicate the occurrence of accumulating hail. Our results aim to assist forecasters in recognizing and predicting future plowable hailstorms.

The following summarizes the most important results:

- Moist westerly 500-hPa flow of 5–15 m s^{-1} (Fig. 3) combined with postfrontal, low-level upslope flow (Figs. 4 and 5) to produce 0–6 km AGL vertically averaged wind speeds of 2–12 m s^{-1} (Table 2). These weak steering winds produced slow storm motions of 6–9 m s^{-1} (Table 1).
- The slow storm motions resulted in unusually long hailfalls that lasted 9.3 min on 3 August, 18.6 min on 9 September and 21 May, and 28.0 min on 22 August at the plowable hail locations (section 5), as estimated from dual-polarization radar data. In contrast, most hail climatologies in the literature report median hailfall durations of 1–7 min (e.g., Changnon 1967; Wojtiw 1975; Paul 1980).
- These unusually long hail durations occurred in anomalously moist environments, with precipitable water values that were 132%–184% of monthly normals (Fig. 8a). The large atmospheric moisture likely further increased the amount of hail that accumulated.
- Three of the four plowable hailstorms were supercell thunderstorms (section 4a). A fourth plowable hail event occurred when a multicell thunderstorm interacted with an outflow boundary to initiate a new convective cell that produced accumulating hail [Fig. 18; section 4b(1)ii].
- Although three of the four storms produced nonaccumulating hail for much of their lifetimes, the

plowable hail occurred during maxima in storm intensity, as evidenced by peaks in 50-dBZ echo-top height of 11–15 km (Fig. 14), maximum column $Z >$ 70 dBZ (Fig. 14), descending columns of Z_{DR} and ρ_{HV} as small as −4 dB (Fig. 15) and 0.4 (Fig. 16), respectively, and BWERs (Fig. 13) in the three supercell thunderstorms. These characteristics were most pronounced in the storms with the largest reported hailstones.

- Large $Z > 70$ dBZ is unusual for storms in which giant hail ($d > 50.8$ mm) was not reported (Ryzhkov et al. 2010), and is likely indicative of the extreme hail mass concentrations.
- The most promising way to detect plowable hail may be to accumulate the radar-derived hail amount over successive radar scans [Eq. (4); section 4b(2)]. This approach is similar to the technique used to detect storms that may produce flash flooding.
- Three of the four thunderstorms had peaks in lightning flash rate that occurred at or near the plowable hail report times (Fig. 21). Graupel is likely the physical connection between increased lightning activity and accumulating hail, since graupel particles serve as both hailstone embryos (Knight and Knight 2001) and charged particles (Williams et al. 1991; Saunders 1993; Takahashi and Miyawaki 2002; Saunders 2008).
- Forecasters report that peaks in the lightning flash rate assist them in the warning decision-making process (Darden et al. 2010), and thus peaks in flash rate that coincide with accumulating hail may help forecasters to identify these events.

The relationships among the synoptic weather, radar, and lightning variables analyzed herein are based on four plowable hailstorms. Future work will focus on additional analyses using a larger sample of hailstorms so that statistical relationships can be determined. In addition, establishing a database of reliable hail-depth observations, particularly in rural areas, would assist in validating relationships between the radar and lightning variables and accumulating hail. Nevertheless, forecasters can use the results from this initial study to detect similar synoptic weather patterns that may be conducive to plowable hailstorms. Once it is known that the weather pattern favors storms with accumulating hail, the dual-polarization radar and lightning data can be used together to determine the likelihood that a particular storm will result in substantial hail accumulations.

Acknowledgments. We thank the employees of the National Weather Service Forecast Office in Boulder for providing valuable feedback on this study. We also thank Mike Dixon (NCAR) for his assistance in using the Radx C++ software package for radar data processing, and Scott Ellis (NCAR) for his help in using Solo II to view and edit the radar data. Feedback from three anonymous reviewers greatly improved an earlier version of this manuscript. This material is based upon work supported by the National Science Foundation Graduate Research Fellowship program under DGE-1144083. A portion of this research was performed while EAK held a National Research Council Research Associateship Award at the Earth System Research Laboratory and the Atlantic Oceanographic and Meteorological Laboratory.

REFERENCES

Aydin, K., T. A. Seliga, and V. Balaji, 1986: Remote sensing of hail with a dual-linear polarization radar. *J. Climate Appl. Meteor.*, **25**, 1475–1484, doi:10.1175/1520-0450(1986)025<1475:RSOHWA>2.0.CO;2.

Balakrishnan, N., and D. S. Zrnić, 1990a: Estimation of rain and hail rates in mixed-phase precipitation. *J. Atmos. Sci.*, **47**, 565–583, doi:10.1175/1520-0469(1990)047<0565:EORAHR>2.0.CO;2.

——, and ——, 1990b: Use of polarization to characterize precipitation and discriminate large hail. *J. Atmos. Sci.*, **47**, 1525–1540, doi:10.1175/1520-0469(1990)047<1525:UOPTCP>2.0.CO;2.

Berthet, C., E. Wesolek, J. Dessens, and J. L. Sanchez, 2013: Extreme hail day climatology in southwestern France. *Atmos. Res.*, **123**, 139–150, doi:10.1016/j.atmosres.2012.10.007.

Brandes, E. A., G. Zhang, and J. Vivekanandan, 2002: Experiments in rainfall estimation with a polarimetric radar in a subtropical environment. *J. Appl. Meteor.*, **41**, 674–685, doi:10.1175/1520-0450(2002)041<0674:EIREWA>2.0.CO;2.

Bringi, V. N., and V. Chandrasekar, 2001: *Polarimetric Doppler Weather Radar: Principles and Applications*. Cambridge University Press, 636 pp.

Browning, K. A., 1963: The growth of large hail within a steady updraught. *Quart. J. Roy. Meteor. Soc.*, **89**, 490–506, doi:10.1002/qj.49708938206.

——, 1965: Some inferences about the updraft within a severe local storm. *J. Atmos. Sci.*, **22**, 669–677, doi:10.1175/1520-0469(1965)022<0669:SIATUW>2.0.CO;2.

——, and F. H. Ludlam, 1962: Airflow in convective storms. *Quart. J. Roy. Meteor. Soc.*, **88**, 117–135, doi:10.1002/qj.49708837602.

——, and G. B. Foote, 1976: Airflow and hail growth in supercell storms and some implications for hail suppression. *Quart. J. Roy. Meteor. Soc.*, **102**, 499–533, doi:10.1002/qj.49710243303.

Carey, L. D., and S. A. Rutledge, 1996: A multiparameter radar case study of the microphysical and kinematic evolution of a lightning producing storm. *Meteor. Atmos. Phys.*, **59**, 33–64, doi:10.1007/BF01032000.

——, and ——, 1998: Electrical and multiparameter radar observations of a severe hailstorm. *J. Geophys. Res.*, **103**, 13 979–14 000, doi:10.1029/97JD02626.

Changnon, S. A., Jr., 1967: Areal-temporal variations of hail intensity in Illinois. *J. Appl. Meteor.*, **6**, 536–541, doi:10.1175/1520-0450(1967)006<0536:ATVOHI>2.0.CO;2.

Chappell, C. F., and D. M. Rodgers, 1988: Meteorological analysis of the Cheyenne, Wyoming, flash flood and hailstorm of 1 August 1985. NOAA Tech. Rep. ERL 435-FSL 1, 51 pp.

[Available online at http://docs.lib.noaa.gov/noaa_documents/OAR/FSL/TR_ERL-435_FSL-1.pdf.]

Darden, C. B., D. J. Nadler, B. C. Carcione, R. J. Blakeslee, G. T. Stano, and D. E. Buechler, 2010: Utilizing total lightning information to diagnose convective trends. *Bull. Amer. Meteor. Soc.*, **91**, 167–175, doi:10.1175/2009BAMS2808.1.

Das, P., 1962: Influence of the wind shear on the growth of hail. *J. Atmos. Sci.*, **19**, 407–414, doi:10.1175/1520-0469(1962)019<0407:IOWSOT>2.0.CO;2.

Deierling, W., and W. A. Petersen, 2008: Total lightning activity as an indicator of updraft characteristics. *J. Geophys. Res.*, **113**, D16210, doi:10.1029/2007JD009598.

——, ——, J. Latham, S. Ellis, and H. J. Christian, 2008: The relationship between lightning activity and ice fluxes in thunderstorms. *J. Geophys. Res.*, **113**, D15210, doi:10.1029/2007JD009700.

Depue, T. K., P. C. Kennedy, and S. A. Rutledge, 2007: Performance of the hail differential reflectivity (H_{DR}) polarimetric hail indicator. *J. Appl. Meteor. Climatol.*, **46**, 1290–1301, doi:10.1175/JAM2529.1.

Dessens, H., 1960: Severe hailstorms are associated with very strong winds between 6,000 and 12,000 meters. *Physics of Precipitation*, *Geophys. Monogr.*, No. 5, Amer. Geophys. Union, 333–338.

Dessens, J., 1986: Hail in southwestern France. I: Hailfall characteristics and hailstorm environment. *J. Climate Appl. Meteor.*, **25**, 35–47, doi:10.1175/1520-0450(1986)025<0035:HISFIH>2.0.CO;2.

Dye, J. E., W. P. Winn, J. J. Jones, and D. W. Breed, 1989: The electrification of New Mexico thunderstorms: 1. Relationship between precipitation development and the onset of electrification. *J. Geophys. Res.*, **94**, 8643–8656, doi:10.1029/JD094iD06p08643.

Emersic, C., P. L. Heinselman, D. R. MacGorman, and E. C. Bruning, 2011: Lightning activity in a hail-producing storm observed with phased-array radar. *Mon. Wea. Rev.*, **139**, 1809–1825, doi:10.1175/2010MWR3574.1.

Friedrich, K., E. A. Kalina, J. D. Aikins, D. Gochis, and R. Rasmussen, 2016a: Precipitation and cloud structures of intense rain during the 2013 Great Colorado Flood. *J. Hydrometeor.*, **17**, 27–52, doi:10.1175/JHM-D-14-0157.1.

——, ——, ——, M. Steiner, D. Gochis, P. A. Kucera, K. Ikeda, and J. Sun, 2016b: Raindrop size distribution and rain characteristics during the 2013 Great Colorado Flood. *J. Hydrometeor.*, **17**, 53–72, doi:10.1175/JHM-D-14-0184.1.

Giuli, D., M. Gherardelli, A. Freni, T. A. Seliga, and K. Aydin, 1991: Rainfall and clutter discrimination by means of dual-linear polarization radar measurements. *J. Atmos. Oceanic Technol.*, **8**, 777–789, doi:10.1175/1520-0426(1991)008<0777:RACDBM>2.0.CO;2.

Gochis, D. J., and Coauthors, 2015: The Great Colorado Flood of September 2013. *Bull. Amer. Meteor. Soc.*, **96**, 1461–1487, doi:10.1175/BAMS-D-13-00241.1.

Goodman, S. J., and Coauthors, 2005: The North Alabama Lightning Mapping Array: Recent severe storm observations and future prospects. *Atmos. Res.*, **76**, 423–437, doi:10.1016/j.atmosres.2004.11.035.

Grahame, N., B. Riddaway, A. Eadie, B. Hall, and E. McCallum, 2009: Exceptional hailstorm hits Ottery St Mary on 30 October 2008. *Weather*, **64** (10), 255–263, doi:10.1002/wea.458.

Gremillion, M. S., and R. E. Orville, 1999: Thunderstorm characteristics of cloud-to-ground lightning at the Kennedy Space Center, Florida: A study of lightning initiation signatures as indicated by the WSR-88D. *Wea. Forecasting*, **14**, 640–649, doi:10.1175/1520-0434(1999)014<0640:TCOCTG>2.0.CO;2.

Herzegh, P. H., and A. R. Jameson, 1992: Observing precipitation through dual-polarization radar measurements. *Bull. Amer. Meteor. Soc.*, **73**, 1365–1374, doi:10.1175/1520-0477(1992)073<1365:OPTDPR>2.0.CO;2.

Heymsfield, A. J., and K. M. Miller, 1988: Water vapor and ice mass transported into the anvils of CCOPE thunderstorms: Comparison with storm influx and rainout. *J. Atmos. Sci.*, **45**, 3501–3514, doi:10.1175/1520-0469(1988)045<3501:WVAIMT>2.0.CO;2.

Hubbert, J. C., and V. N. Bringi, 2000: The effects of three-body scattering on differential reflectivity signatures. *J. Atmos. Oceanic Technol.*, **17**, 51–61, doi:10.1175/1520-0426(2000)017<0051:TEOTBS>2.0.CO;2.

Illingworth, A., and T. Blackman, 2002: The need to represent raindrop size spectra as normalized gamma distributions for the interpretation of polarization radar observations. *J. Appl. Meteor.*, **41**, 286–297, doi:10.1175/1520-0450(2002)041<0286:TNTRRS>2.0.CO;2.

Kennedy, P. C., S. A. Rutledge, B. Dolan, and E. Thaler, 2014: Observations of the 14 July 2011 Fort Collins hailstorm: Implications for WSR-88D-based hail detection and warnings. *Wea. Forecasting*, **29**, 623–638, doi:10.1175/WAF-D-13-00075.1.

Knight, C. A., and N. C. Knight, 2001: Hailstorms. *Severe Convective Storms, Meteor. Monogr.*, No. 50, Amer. Meteor. Soc., 223–249.

——, P. T. Schlatter, and T. W. Schlatter, 2008: An unusual hailstorm on 24 June 2006 in Boulder, Colorado. Part II: Low-density growth of hail. *Mon. Wea. Rev.*, **136**, 2833–2848, doi:10.1175/2008MWR2338.1.

Kumjian, M. R., and A. V. Ryzhkov, 2008: Polarimetric signatures in supercell thunderstorms. *J. Appl. Meteor. Climatol.*, **47**, 1940–1961, doi:10.1175/2007JAMC1874.1.

——, J. Picca, S. Ganson, A. Ryzhkov, and D. Zrnić, 2010: Three body scattering signatures in polarimetric radar data. NOAA/NSSL Tech. Rep., 12 pp. [Available online at http://www.nssl.noaa.gov/publications/wsr88d_reports/FINAL_TBSS.doc.]

Lee, W.-C., R. E. Carbone, and R. M. Wakimoto, 1992: The evolution and structure of a "bow-echo–microburst" event. Part I: The microburst. *Mon. Wea. Rev.*, **120**, 2188–2210, doi:10.1175/1520-0493(1992)120<2188:TEASOA>2.0.CO;2.

Lesins, G. B., and R. List, 1986: Sponginess and drop shedding of gyrating hailstones in a pressure-controlled icing wind tunnel. *J. Atmos. Sci.*, **43**, 2813–2825, doi:10.1175/1520-0469(1986)043<2813:SADSOG>2.0.CO;2.

Longley, R. W., and C. E. Thompson, 1965: A study of causes of hail. *J. Appl. Meteor.*, **4**, 69–82, doi:10.1175/1520-0450(1965)004<0069:ASOCOH>2.0.CO;2.

Marshall, J. S., and W. M. K. Palmer, 1948: The distribution of raindrops with size. *J. Meteor.*, **5**, 165–166, doi:10.1175/1520-0469(1948)005<0165:TDORWS>2.0.CO;2.

Marwitz, J. D., and E. X. Berry, 1971: The airflow within the weak echo region of an Alberta hailstorm. *J. Appl. Meteor.*, **10**, 487–492, doi:10.1175/1520-0450(1971)010<0487:TAWTWE>2.0.CO;2.

——, A. H. Auer Jr., and D. L. Veal, 1972: Locating the organized updraft on severe thunderstorms. *J. Appl. Meteor.*, **11**, 236–238, doi:10.1175/1520-0450(1972)011<0236:LTOUOS>2.0.CO;2.

McCaul, E. W., Jr., J. C. Bailey, J. Hall, S. J. Goodman, R. J. Blakeslee, and D. E. Buechler, 2005: A flash clustering algorithm for North Alabama Lightning Mapping Array data. Preprints, *Conf. on Meteorological Applications of Lightning Data*, San Diego, CA, Amer. Meteor. Soc., 5.3.

[Available online at https://ams.confex.com/ams/Annual2005/techprogram/paper_84373.htm.]

——, S. J. Goodman, K. M. LaCasse, and D. J. Cecil, 2009: Forecasting lightning threat using cloud-resolving model simulations. *Wea. Forecasting*, **24**, 709–729, doi:10.1175/2008WAF2222152.1.

Nelson, S. P., 1983: The influence of storm flow structure on hail growth. *J. Atmos. Sci.*, **40**, 1965–1983, doi:10.1175/1520-0469(1983)040<1965:TIOSFS>2.0.CO;2.

OFCM, 2013: Doppler radar meteorological observations: Part A. System concepts, responsibilities, and procedures. Federal Meteorological Handbook No. 11, FCM-H11A-2013, Office of the Federal Coordinator for Meteorological Services and Supporting Research, 21 pp. [Available online at http://www.ofcm.gov/fmh11/fmh11.htm.]

Pappas, J. J., 1962: A simple yes–no hail forecasting technique. *J. Appl. Meteor.*, **1**, 353–354, doi:10.1175/1520-0450(1962)001<0353:ASYNHF>2.0.CO;2.

Park, H., A. V. Ryzhkov, D. S. Zrnić, and K. Kim, 2009: The hydrometeor classification algorithm for the polarimetric WSR-88D: Description and application to an MCS. *Wea. Forecasting*, **24**, 730–748, doi:10.1175/2008WAF2222205.1.

Paul, A. H., 1980: Hailstorms in southern Saskatchewan. *J. Appl. Meteor.*, **19**, 305–313, doi:10.1175/1520-0450(1980)019<0305:HISS>2.0.CO;2.

Pereyra, R. G., E. E. Avila, N. E. Castellano, and C. P. R. Saunders, 2000: A laboratory study of graupel charging. *J. Geophys. Res.*, **105**, 20 803–20 812, doi:10.1029/2000JD900244.

Pruppacher, H. R., and J. D. Klett, 1997: *Microphysics of Clouds and Precipitation*. 2nd ed. Kluwer Academic, 954 pp.

Rasmussen, R. M., and A. J. Heymsfield, 1987: Melting and shedding of graupel and hail. Part I: Model physics. *J. Atmos. Sci.*, **44**, 2754–2763, doi:10.1175/1520-0469(1987)044<2754:MASOGA>2.0.CO;2.

Rison, W., P. R. Krehbiel, R. J. Thomas, D. Rodeheffer, and B. Fuchs, 2012: The Colorado Lightning Mapping Array. *2012 Fall Meeting*, San Francisco, CA, Amer. Geophys. Union, AE23B-0319. [Available online at http://fallmeeting.agu.org/2012/eposters/eposter/ae23b-0319.]

Rosenfeld, D., D. B. Wolff, and D. Atlas, 1993: General probability-matched relations between radar reflectivity and rain rate. *J. Appl. Meteor.*, **32**, 50–72, doi:10.1175/1520-0450(1993)032<0050:GPMRBR>2.0.CO;2.

Rudlosky, S. D., and H. E. Fuelberg, 2013: Documenting storm severity in the mid-Atlantic region using lightning and radar information. *Mon. Wea. Rev.*, **141**, 3186–3202, doi:10.1175/MWR-D-12-00287.1.

Ryzhkov, A., D. Zrnić, J. Krause, M. Kumjian, and S. Ganson, 2010: Discrimination between large and small hail: Final report. NOAA/NSSL Tech. Rep., 18 pp. [Available online at https://www.nssl.noaa.gov/publications/wsr88d_reports/FINAL_HailSize.doc.]

——, M. R. Kumjian, S. M. Ganson, and A. P. Khain, 2013a: Polarimetric radar characteristics of melting hail. Part I: Theoretical simulations using spectral microphysical modeling. *J. Appl. Meteor. Climatol.*, **52**, 2849–2870, doi:10.1175/JAMC-D-13-073.1.

——, ——, ——, and P. Zhang, 2013b: Polarimetric radar characteristics of melting hail. Part II: Practical implications. *J. Appl. Meteor. Climatol.*, **52**, 2871–2886, doi:10.1175/JAMC-D-13-074.1.

Saunders, C. P. R., 1993: A review of thunderstorm electrification processes. *J. Appl. Meteor.*, **32**, 642–655, doi:10.1175/1520-0450(1993)032<0642:AROTEP>2.0.CO;2.

——, 2008: Charge separation mechanisms in clouds. *Space Sci. Rev.*, **137**, 335–353, doi:10.1007/s11214-008-9345-0.

——, and I. M. Brooks, 1992: The effects of high liquid water content on thunderstorm charging. *J. Geophys. Res.*, **97**, 14 671–14 676, doi:10.1029/92JD01186.

Schlatter, P. T., T. W. Schlatter, and C. A. Knight, 2008: An unusual hailstorm on 24 June 2006 in Boulder, Colorado. Part I: Mesoscale setting and radar features. *Mon. Wea. Rev.*, **136**, 2813–2832, doi:10.1175/2008MWR2337.1.

Schlatter, T. W., and N. Doesken, 2010: Deep hail: Tracking an elusive phenomenon. *Weatherwise*, **63** (5), 35–41, doi:10.1080/00431672.2010.503841.

Schultz, C. J., W. A. Petersen, and L. D. Carey, 2009: Preliminary development and evaluation of lightning jump algorithms for the real-time detection of severe weather. *J. Appl. Meteor. Climatol.*, **48**, 2543–2563, doi:10.1175/2009JAMC2237.1.

Scott, G. D., and D. M. Kilgour, 1969: The density of random close packing of spheres. *J. Phys. D: Appl. Phys.*, **2**, 863–866, doi:10.1088/0022-3727/2/6/311.

Shafer, M. A., D. R. MacGorman, and F. H. Carr, 2000: Cloud-to-ground lightning throughout the lifetime of a severe storm system in Oklahoma. *Mon. Wea. Rev.*, **128**, 1798–1816, doi:10.1175/1520-0493(2000)128<1798:CTGLTT>2.0.CO;2.

Snyder, J. C., H. B. Bluestein, G. Zhang, and S. J. Frasier, 2010: Attenuation correction and hydrometeor classification of high-resolution, X-band, dual-polarized mobile radar measurements in severe convective storms. *J. Atmos. Oceanic Technol.*, **27**, 1979–2001, doi:10.1175/2010JTECHA1356.1.

Srivastava, R. C., 1987: A model of intense downdrafts driven by the melting and evaporation of precipitation. *J. Atmos. Sci.*, **44**, 1752–1774, doi:10.1175/1520-0469(1987)044<1752:AMOIDD>2.0.CO;2.

Takahashi, T., and K. Miyawaki, 2002: Reexamination of riming electrification in a wind tunnel. *J. Atmos. Sci.*, **59**, 1018–1025, doi:10.1175/1520-0469(2002)059<1018:RROREIA>2.0.CO;2.

Tessendorf, S. A., L. J. Miller, K. C. Wiens, and S. A. Rutledge, 2005: The 29 June 2000 supercell observed during STEPS. Part I: Kinematics and microphysics. *J. Atmos. Sci.*, **62**, 4127–4150, doi:10.1175/JAS3585.1.

——, K. C. Wiens, and S. A. Rutledge, 2007: Radar and lightning observations of the 3 June 2000 electrically inverted storm from STEPS. *Mon. Wea. Rev.*, **135**, 3665–3681, doi:10.1175/2006MWR1953.1.

Thomas, R. J., P. R. Krehbiel, W. Rison, S. J. Hunyady, W. P. Winn, T. Hamlin, and J. Harlin, 2004: Accuracy of the Lightning Mapping Array. *J. Geophys. Res.*, **109**, D14207, doi:10.1029/2004JD004549.

Vincent, B. R., L. D. Carey, D. Schneider, K. Keeter, and R. Gonski, 2003: Using WSR-88D reflectivity data for the prediction of cloud-to-ground lightning: A central North Carolina study. *Natl. Wea. Dig.*, **27**, 35–44.

Vivekanandan, J., S. M. Ellis, R. Oye, D. S. Zrnić, A. V. Ryzhkov, and J. Straka, 1999: Cloud microphysics retrieval using S-band dual-polarization radar measurements. *Bull. Amer. Meteor. Soc.*, **80**, 381–388, doi:10.1175/1520-0477(1999)080<0381:CMRUSB>2.0.CO;2.

Weisman, M. L., and J. B. Klemp, 1984: The structure and classification of numerically simulated convective storms in directionally varying wind shears. *Mon. Wea. Rev.*, **112**, 2479–2498, doi:10.1175/1520-0493(1984)112<2479:TSACON>2.0.CO;2.

Wiens, K. C., 2005: Kinematic, microphysical, and electrical structure and evolution of thunderstorms during the Severe Thunderstorm Electrification and Precipitation Study (STEPS). Ph.D. thesis, Colorado State University, 295 pp.

——, S. A. Rutledge, and S. A. Tessendorf, 2005: The 29 June 2000 supercell observed during steps. Part II: Lightning and charge structure. *J. Atmos. Sci.*, **62**, 4151–4177, doi:10.1175/JAS3615.1.

Williams, E. R., R. Zhang, and J. Rydock, 1991: Mixed-phase microphysics and cloud electrification. *J. Atmos. Sci.*, **48**, 2195–2203, doi:10.1175/1520-0469(1991)048<2195:MPMACE>2.0.CO;2.

——, and Coauthors, 1999: The behavior of total lightning activity in severe Florida thunderstorms. *Atmos. Res.*, **51**, 245–264, doi:10.1016/S0169-8095(99)00011-3.

Wojtiw, L., 1975: Climatic summaries of hailfall in central Alberta (1957–73). Atmospheric Science Rep. 75-1, Alberta Research, Edmonton, AB, Canada, 102 pp.

Xie, B., Q. Zhang, and Y. Wang, 2010: Observed characteristics of hail size in four regions in China during 1980–2005. *J. Climate*, **23**, 4973–4982, doi:10.1175/2010JCLI3600.1.

Zeng, Z., S. E. Yuter, R. A. Houze, and D. E. Kingsmill, 2001: Microphysics of the rapid development of heavy convective precipitation. *Mon. Wea. Rev.*, **129**, 1882–1904, doi:10.1175/1520-0493(2001)129<1882:MOTRDO>2.0.CO;2.

Ziegler, C. L., P. S. Ray, and N. C. Knight, 1983: Hail growth in an Oklahoma multicell storm. *J. Atmos. Sci.*, **40**, 1768–1791, doi:10.1175/1520-0469(1983)040<1768:HGIAOM>2.0.CO;2.

Zrnić, D. S., 1987: Three-body scattering produces precipitation signature of special diagnostic value. *Radio Sci.*, **22**, 76–86, doi:10.1029/RS022i001p00076.